AD-756 906

INVESTIGATION OF SOLID CADMIUM EMBRITTLEMENT IN A-7 AIRCRAFT FAILED SHAFTS AND HORN FRACTURE SURFACES

O. H. Cook, et al

Vought Aeronautics Company

Prepared for:

Air Force Materials Laboratory

January 1973

DISTRIBUTED BY:

NTIS

National Technical Information Service
U. S. DEPARTMENT OF COMMERCE
5285 Port Royal Road, Springfield Va. 22151

AFML-TR-72-249

AD756906

INVESTIGATION OF SOLID CADMIUM EMBRITTLEMENT IN A-7 AIRCRAFT FAILED SHAFTS AND HORN FRACTURE SURFACES

Prepared by:

O. H. Cook
R. E. Duval
C. G. Ford
R. W. White

Vought Aeronautics Company
LTV Aerospace Corporation

TECHNICAL REPORT AFML-TR-72-249

January 1973

Air Force Materials Laboratory
Air Force Systems Command
Wright-Patterson Air Force Base, Ohio

APPROVED FOR PUBLIC RELEASE, DISTRIBUTION UNLIMITED

89

DOCUMENT CONTROL DATA - R & D

(Security classification of title, body of abstract and indexing annotation must be entered when the overall report is classified)

1. ORIGINATING ACTIVITY *(Corporate author)* Vought Aeronautics Company LTV Aerospace Corporation Dallas, Texas 75222	2a. REPORT SECURITY CLASSIFICATION UNCLASSIFIED 2b. GROUP

3. REPORT TITLE

Investigation of Solid Cadmium Embrittlement in A-7 Aircraft Failed Shafts and Horn Fracture Surfaces

4. DESCRIPTIVE NOTES *(Type of report and inclusive dates)*

Final Report 1 April 1972 through 15 May 1973

5. AUTHOR(S) *(First name, middle initial, last name)*

O. H. Cook, R. E. Duval, C. G. Ford, R. W. White

6. REPORT DATE	7a. TOTAL NO. OF PAGES	7b. NO. OF REFS
October 1972	86	3

8a. CONTRACT OR GRANT NO. F33615-72-C-1609	9a. ORIGINATOR'S REPORT NUMBER(S) AFML-TR-72-249
b. PROJECT NO. 7381	
c. Task No. 738107	9b. OTHER REPORT NO(S) *(Any other numbers that may be assigned this report)*
d. Work Unit No. 73810738	2-50110/3R-3062

10. DISTRIBUTION STATEMENT

Approved for Public Release, Distribution Unlimited.

11. SUPPLEMENTARY NOTES	12. SPONSORING MILITARY ACTIVITY
	Air Force Materials Laboratory (MXA) Air Force Systems Command Wright-Patterson AFB, Ohio 45433

13. ABSTRACT

Solid cadmium embrittlement, which was first discovered as the cause of failures in titanium fasteners, can also cause cracking in high strength steels. The conditions which must be present for initiation of this phenomenon are:

- o There must be intimate contact between the cadmium and steel.
- o The steel must be heat treated to ultimate strength levels of 200 Ksi or over.
- o A tensile stress must act parallel to the surfaces exposed to the cadmium.

The A-7 Aircraft horizontal tail actuator shaft and horn assembly meet these conditions; therefore, an investigation was made to determine the possible presence of cadmium as a contributor to failure on six shaft and one horn fracture surfaces. Metallography, fractography, microprobe analysis, Auger electron spectroscopy, and other experimental means were utilized in the investigation. Induced solid cadmium embrittlement failures were characterized and used as a control in the analysis.

This investigation conclusively proved that solid cadmium embrittlement was not the cause of failure, and that hydrogen embrittlement was the failure mode. This indicates that hydrogen embrittlement cracking will occur in cadmium plated high strength steels where moisture is present at lower stress levels than solid cadmium embrittlement.

Details of illustrations in this document may be better studied on microfiche.

Unclassified

Security Classification

14. KEY WORDS	LINK A		LINK B		LINK C	
	ROLE	WT	ROLE	WT	ROLE	WT
Cadmium						
Embrittlement						
High Strength Steels						

I b

Unclassified

Security Classification

AFML-TR-72-249

INVESTIGATION OF SOLID CADMIUM EMBRITTLEMENT IN A-7 AIRCRAFT FAILED SHAFTS AND HORN FRACTURE SURFACES

Prepared by:

O. H. Cook
R. E. Duval
C. G. Ford
R. W. White

Vought Aeronautics Company
LTV Aerospace Corporation

APPROVED FOR PUBLIC RELEASE; DISTRIBUTION UNLIMITED

I.a

FOREWORD

This report was prepared by the Engineering Materials Department of Vought Aeronautics Company under Air Force Contract F33615-72-C-1609. This report covers work performed from 1 April 1972 to 1 October 1972. The work was administered by Fred H. Meyer, Jr., Project Engineer under the direction of the Air Force Materials Laboratory, Air Force Systems Command, Wright-Patterson AFB, Ohio 45433.

This report covers an investigation to determine whether failures in A-7 aircraft horizontal tail actuator horn and shaft assemblies could be attributable to the solid cadmium embrittlement phenomenon.

Vought Aeronautics Company (VAC) performed the work with Mr. O. H. Cook as Principal Investigator, under the administration of Mr. A. E. Hohman, Supervisor, Engineering Materials Department.

The manuscript was released by the authors in October 1972 for publication as an Air Force Materials Laboratory (AFML) Technical Report. This technical report has been reviewed and is approved.

D. A. SHINN, Chief
Aeronautical Systems Branch
Systems Support Division
Air Force Materials Laboratory

ABSTRACT

Solid cadium embrittlement, which was first discovered as the cause of failures in titanium fasteners, can also cause cracking in high strength steels. The conditions which must be present for initiation of this phenomenon are:

- There must be intimate contact between the cadmium and steel.
- The steel must be heat treated to ultimate strength levels of 200 KSi or over.
- A tensile stress must act parallel to the surfaces exposed to the cadmium.

The A-7 aircraft horizontal tail actuator shaft and horn assembly meet these conditions; therefore, an investigation was made to determine the possible presence of cadmium as a contributor to failure on six shaft and one horn fracture surfaces. Metallography, fractography, microprobe analysis, Auger electron spectroscopy, and other experimental means were utilized in the investigation. Induced solid cadmium embrittlement failures were characterized and used as a control in the analysis.

This investigation conclusively proved that solid cadmium embrittlement was not the cause of failure, and that hydrogen embrittlement was the failure mode. This indicates that hydrogen embrittlement cracking will occur in cadmium plated high strength steels where moisture is present at lower stress levels than solid cadmium embrittlement.

Page iv is blank.

TABLE OF CONTENTS

Page

FIGURES

FIGURES

FIGURES

FIGURES

TABLES

SECTION I

INTRODUCTION

This report covers the investigation of failures in A-7 aircraft horizontal tail actuator horn and shaft assemblies to determine whether the solid cadmium embrittlement phenomenon was the mechanism causing any of these failures.

The objective of this program was twofold:

- Determine whether solid cadmium embrittlement was the failure mode on any parts from a large representative sample meeting the criteria for this type of failure.

- Develop the detailed failure profile and establish the characteristics of solid cadmium embrittlement.

Solid cadmium embrittlement, a recently discovered mechanism, was first defined for titanium alloys. Fastener manufacturers and users isolated the mechanism when an inordinate number of failures appeared in cadmium plated titanium fasteners. Standard Pressed Steel and Hi-Shear Corporation conducted investigations in this area, and Boeing Company did extensive work to further explain the phenomenon. The Defense Metals Information Center at Battelle Memorial Institute held a meeting in October, 1969 to discuss this problem. Several companies, in addition to the above mentioned, cited cases of cadmium influenced cracking in titanium, and included Grumman, McDonnell Douglas and Lockheed. The Boeing work demonstrated that the presence of cadmium at temperatures as low as 100°F caused cracking (Reference A). The Boeing research was extended into steel alloys (Reference B). The main conclusions drawn from these efforts to define the solid cadmium embrittlement phenomenon are basically the same for the titanium and steel alloys investigated.

All the facts are not known on cadmium embrittlement cracking; but the following requirements appear to be valid for steel:

- Intimate contact between the cadmium and steel is necessary.

- The steel must be heat treated to ultimate tensile strength levels of 200 Ksi or over.

- A tensile stress must act parallel to the surfaces exposed to cadmium.

- Brittle intergranular and transgranular cleavage fracture paths are formed.

- Cracking becomes more severe as the exposure temperature is increased, indicating that the cadmium diffusion rate is a controlling factor.

In a recent metallurgical investigation (Reference C) into the cause of brittle intergranular cracks at taper-pin holes in the horn and shaft of an A-7 aircraft horizontal tail actuator, it was concluded that the cause of failure in the actuator shaft was solid cadmium embrittlement. In the conclusions of this report, related to the shaft failure, it was recommended that correlating evidence was needed from similar failures. Because other failure surfaces similar to the one investigated were available from the A-7 horizontal tail actuator, this was deemed an excellent source of specimens for an in-depth investigation for the possible presence of solid cadmium embrittlement. Another reason supporting the choice of these parts for an investigation was that they fit the prerequisites established for making this phenomenon operative.

The shaft and horn assembly is made up of the horn (P/N 15-160059), which is attached to the shaft (P/N 15-160003) by eight taper-pins (P/N 15-160513). The cracks have initiated at cadmium plated taper-pin holes in the horn and shaft. Typical examples are shown in Figures 1 and 2. The horn is 4340 steel heat treated to an ultimate tensile strength minimum of 200 Ksi, and the shaft is 4340 steel heat treated to an ultimate tensile strength minimum of 260 Ksi. The shaft and horn holes are cadmium plated, and the assembly between the shaft and horn accomplished by torquing the taper-pins through the matching holes. The torquing action generates a tensile stress acting parallel to the steel surfaces exposed to cadmium, as well as forcing intimate contact at the cadmium/steel interface. The steel is heat treated to an ultimate tensile strength of 200 Ksi or higher; thus the criteria for generation of solid cadmium embrittlement appear to be met when the taper-pins are installed.

Failure analyses of shaft and horn parts, which have failure modes that appear similar to the shaft reported to be solid cadmium embrittlement, have been conducted at Vought Aeronautics Company. These failures have been attributed to hydrogen embrittlement due to (1) sub-surface initiation and (2) the intergranular fracture mode. As the solid cadmium embrittlement mechanism was not defined at the time of these analyses, it was not suspect, which was another item supporting further investigation into these failures.

In summary, the evidence from (1) these analyses, (2) the one reported cadmium service failure, and (3) the existence of the basic prerequisites for solid cadmium embrittlement made the A-7 shaft and horn fracture surfaces excellent subjects for this research.

SECTION II

TEST PROGRAM

Six shaft failure surfaces and one horn failure surface were examined for the presence of solid cadmium embrittlement. These program test parts are identified in Table I. The analysis procedure consisted of the following:

- Standard samples simulating the actual conditions which exist during solid cadmium embrittlement were prepared and evaluated as a standard of comparison.
- Metallographic studies were made on fracture surfaces and cross sections using polarized light to detect cadmium.
- The fractures were examined using carbon replicas and scanning electron microscopy to establish the failure mode, to look for foreign material and to confirm the findings of original analysis reports.
- Electron probe analysis was conducted on fracture faces for the presence of cadmium at the surface, crack root, and progressively away from the surface to determine if a gradient resulting from the diffusion mechanism existed.

Other pertinent data such as mechanical properties, microstructural features, and corrosion were correlated with the above data to develop the detailed failure profile and cadmium embrittlement characteristics.

TABLE I LIST OF PARTS TESTED

Part	Aircraft	Part Service Number	Test Report
Shaft	A7B 137	362	69-66
Shaft	A7B 181	144	69-06
Shaft	A7D 8	138	69-06
Shaft	A7B 121	0086	71-001
Shaft	A7B 107	0070	69-135
Shaft	A7B 183	0095	69-13
Horn	A7B 183	0095	69-005

1. SOLID CADMIUM EMBRITTLEMENT SIMULATION TESTS

Two methods were utilized to induce solid cadmium embrittlement failures for use as a standard of comparison with the A-7 aircraft failed parts. The first method was similar to that used in Reference A where the investigators reported successful inducement of cadmium embrittlement. Figure 3 shows the pressure plate and loading fixture. Standard 0.250-in. diameter round tensile specimens heat treated to 260 Ksi ultimate tensile strength were cadmium plated using the vacuum cadmium process and a low embrittlement process (Ti-Cd). The two plating processes were evaluated to determine any differences in mechanism between the two, particularly as to any added effect of the electrochemical process.

The specimens were stressed at 200 Ksi at room temperature in dead weight loading in the setup shown in Figure 5. The pressure plate was then affixed to the text specimen using 80 in-lb torque on the bolts. This assembly was exposed at 400°F ±10° for 20 hours, examined for cracks, and then loaded at room temperature to failure.

The above procedure was performed on two vacuum cadmium and two low embrittlement cadmium plated specimens. Two other vacuum cadmium plated specimens were tested statically to serve as controls.

Following the mechanical testing the fractures were subjected to rigorous failure analysis. The procedure used was as follows:

- Photographs were taken of the test specimens before and after static testing.

- Detailed pictures were taken showing the fracture surfaces. These were made using light photography and also using the scanning electron microscope.

- A comparison photograph was taken showing the variation in reduction in area between the control and embrittled specimens.

- Examination of the fracture topography at high magnification was carried out utilizing both transmission electron microscopy of carbon replicas and scanning electron microscopy of the actual fracture surface. Micrographs were taken showing the results obtained by both techniques.

- An induced failure was cross sectioned through one of the crack origins. Then the section was prepared for examination using standard metallographic procedures. Photomicrographs were then taken showing the results of the microstructural analysis.

The second induced embrittlement test method simulated the conditions present in the A-7 shaft and horn assembly. The assembly was made between shaft and horn segments, shown in Figure 4 using production taper-pins.

Vacuum cadmium plating was employed, as is the case with all production parts. In the test 1,200 in.-lb of torque was applied to the taper-pin assembly. The maximum torque called out on the part drawings is 690 in.-lb; but to account for overtorquing, 1,200 in.-lb was applied. These test assemblies were then exposed at 400°F ±10° for 20 hours and examined as follows:

- The specimens were disassembled and examined visually, then macroscopically and magnaflux inspected.

- The shaft portion of the specimen (260,000 psi) was cut, leaving 0.2 inch of material around the hole to facilitate breaking the specimen. The large part of the tapered pin was driven into the hole causing failure. The fracture surface was examined for cadmium-induced cracking, and photographed.

2. METALLOGRAPHIC EXAMINATION AND FRACTOGRAPHY

The fracture surfaces of both the cadmium induced and service failures were examined to determine the origins. The specimens were sectioned through the origins and prepared for metallurgical examinations. The metallographic specimens were examined before and after etching using bright field and polarized light.

Examination of the fracture topography at high magnification was carried out utilizing transmission electron microscopy of carbon replicas and scanning electron microscopy of the actual fracture surface.

3. ELECTRON MICROPROBE STUDIES

a. Introduction

The electron microprobe provides analysis of microscopic areas of the surface layer of solid specimens. This is accomplished by focusing a very fine beam of high energy electrons onto a selected surface area.

Interaction of the electrons with matter at the surface produces a variety of effects, some of which can be detected, measured, and related to sample composition:

- X-rays emitted include characteristic lines of all elements present on the surface. By use of an x-ray spectrometer, these lines can be isolated and measured.

- Some high-energy electrons are backscattered from the surface.

- Lower-energy electrons, called secondary electrons, are emitted by the surface.

- Surface conductivity gives rise to an effect called specimen current, which can be monitored at the point of electron impact.

All of these effects can be measured with varying degrees of accuracy at a number of points on the surface simply by moving the specimen. Or the beam can be scanned over a small area (a few hundred microns square) by means of an electronic or mechanical scanning device. After amplification, the detected signal can be used to modulate the intensity of an oscilloscope beam scanning in synchronism with the electron beam. In this way a distribution map of the surface can be prepared showing specimen current, backscattered and/or secondary electrons, or the x-rays from some selected element.

In addition, distribution curves for a given element along a selected straight line can be prepared by photographically monitoring the x-ray concentration as a function of distance of electron beam travel along the line.

b. Experimental Procedure

In this work two microprobes were used, a CAMECA Model CEC 27-101 and the Model ARL-SM probe at Texas Instruments, Dallas, Texas. This was done to make full use of differences in working distance and in x-ray take-off angle (57 degrees for the ARL probe versus 18 degrees for the CAMECA probe) to optimize detection of x-rays on the relatively rough fracture surfaces. Thus the two instruments serve as checks against each other to ensure that recorded surface effects are real.

The primary origin area of each crack surface, having been determined microscopically, was examined on the ARL probe. Distribution maps were recorded for backscattered electrons, specimen current, secondary electrons, and cadmium concentration on each of the six shaft fractures and the one horn fracture. In addition, a cadmium concentration profile through each origin at a right angle to the cadmium-plated tapered pin hole surface was recorded. Point counts for cadmium were determined, beginning near each cadmium-plated surface edge and moving in from that edge along the fracture surface. Point counts were made in duplicate, recording to a constant total of 4,000 pulses at each location. All x-ray measurements on the ARL probe were made using the L beta 1 peak.

The origins were examined in a similar manner on the CAMECA probe. Distribution maps were recorded for backscattered and secondary electrons and for cadmium concentration. Point counts for cadmium were again determined as a function of distance along the fracture surface from the plated hole edge. X-ray measurements were made using the L alpha 1 peak.

Thus the several modes employed provide:

- Comparison of results obtained on the two instruments
- A variety of viewpoints of a given area on the same instrument

In this way the maximum information obtainable by using this method was acquired.

4. OTHER TESTS

a. Mechanical Property and Hardness Tests

These tests were conducted on the failed parts as well as on the inducement specimens.

b. Auger Electron Spectroscopy

Studies were initiated as another potential method for cadmium detection.

(1) Introduction

Auger Electro Spectroscopy is a nondestructive technique for chemical analysis with a small depth resolution. Hence, the technique is particularly suited to the study of the top 50 Angstroms of solid surfaces.

The sample surface is bombarded with a beam of electrons in the range up to 5 KeV. An energy analysis of ejected electrons allows detection and identification of the elements present at the sample surface.

Because the contribution of Auger electrons to the total secondary electron spectrum under such circumstances is very small, the Auger signal is usually artificially enhanced. This is accomplished by recording the derivative of the secondary electron distribution. Thus sensitivity and resolution are greatly improved.

The typical Auger spectrum, then, is a plot of dN/dE versus E (energy).

Since only a few of the possible Auger transitions actually occur, spectra of the elements are relatively simple, with little overlap between elements.

The technique is not microscopically selective, in that a relatively large area (approximately one square millimeter) is bombarded and the resultant Auger spectrum reflects average composition of the entire bombarded area.

(2) Experimental Procedure

Two surfaces were examined using Auger spectrometry, one surface with induced cadmium-embrittled failure and one surface with an in-service shaft failure. A small salt crystal was placed over the origin area of each fracture, back a short distance from the cadmium plate. The entire samples were then vacuum plated with gold. Removing the salt crystals gave specimens having surfaces masked with gold, except in the window area protected by the salt crystal.

Both specimens were placed in the Auger Spectrometer and the instrument pumped down. The recorder was centered on the gold peak and the specimen physically moved until the peak showed minimum intensity. This was taken to be the window area, and an Auger spectrum was run at this location.

SECTION III

TEST RESULTS

1. SOLID CADMIUM EMBRITTLEMENT SIMULATION TESTS

Simulation of this mechanism using the test specimen shown in Figure 3 was successful. The specimen, Figure 4, designed to have the same conditions as the failed aircraft parts did not yield any failures in spite of the high torque of 1200 in.-lb. This is considerably in excess of the 690 in.-lb called out on the engineering drawings so it was expected to be effective in inducing cadmium failures if this mechanism were possible with the shaft and horn design.

Examination of the specimens for cracking yielded the following results:

- Visual observation with a light microscope at magnifications ranging from 7X to 60X failed to show evidence of cracking on either type of test specimen.

- Magnetic particle inspection was employed, which yielded strong indications on the tensile bar specimens but none on the taper-pin specimens.

The results of tests outlined in Section III, paragraph 1 are outlined below.

Since examination of the simulation test depicting the actual shaft and horn assembly revealed no cracks, the shaft portion of the specimen was broken by driving the large part of the taper-pin into the hole. Examination of the fractured surface produced exhibited only tension and shear modes of failure. There was no evidence of cadmium-induced cracking. Figures 43 and 44 show the assembled and disassembled specimen and the fracture surface of the shaft portion of the specimen.

Figures 6 and 7 show one of the round tensile specimens after exposure. Note the deformation of the cadmium plate where the pressure plate contacted the specimen.

The embrittled samples generally showed little or no elongation and reduction of area when failed statically. The contrast between embrittled and non-embrittled specimens is shown in Figure 8. Note the necking down of the control sample, while the embrittled samples shows no necking.

The fracture surfaces of the tensile specimens are shown in Figures 9 through 13. The control sample, Figure 9, consisted of a normal cup and cone fracture. Cracking first began at the center of the specimen and propagated radially. Figures 10 and 11 show low embrittlement cadmium samples. Cracking originated from the side of the specimens at one of several crescent

shaped regions on either sample. The crescents were characterized by a crystalline appearance and had a distinct yellow-gold coloration. Several secondary origins were observed on each fracture although the tensile fracture had propagated from a single origin. The vacuum cadmium specimens are shown in Figures 12 and 13. Unlike the low embrittlement cadmium samples, the vacuum cadmium specimens exhibited only one origin on each specimen. Thus it would appear that the low embrittlement cadmium plate was more prone to induce embrittlement than the vacuum cadmium plate. Other variations which were apparent were that the origins on the vacuum cadmium specimens were irregularly shaped and more darkly colored as compared to the low embrittlement cadmium specimens. In all cases however, the origin cracks were located only where the pressure had been applied.

The photomicrographs in Figures 14 through 19 characterize the conditions found in the cadmium-induced failures. Cracks in the low embrittlement cadmium plated specimens were more predominant and severe than in the vacuum deposited cadmium. However, numerous surface initiated cracks were observed in both deposits. These cracks were predominantly intergranular with possible transgranular cleavage depicted as a step pattern in the crack networks. The origins in the low embrittlement cadmium plated specimens generally followed a single plane while the vacuum cadmium tended to branch into several crack fronts. The cross section in Figure 15 shows a cadmium plated surface with a cadmium deposit in the crack. The cadmium was believed to be smeared into the crack during the sectioning and polishing operation. To substantiate this deduction, the metallographic specimen was lightly etched with nital. This resulted in complete removal of the surface smeared cadmium in the cracks while leaving the plated surface only slightly etched and intact. Also electron microprobe analysis of the fracture surfaces revealed no heavy deposits of cadmium such as revealed in the photomicrograph. This aspect will be discussed later.

Electron microscopy revealed several features not apparent at lower magnifications. Figures 20 and 21 show one of the low embrittlement cadmium fractures in detail. Figures 22 and 23 are comparable pictures of a vacuum cadmium sample. In the lower magnification shots, 20 and 22, it is apparent that cracking originated at the steel-cadmium interface and progressed into the steel. The higher magnifications, Figures 21 and 23, show that the origins are somewhat different. The low embrittlement cadmium appears to have generally followed a single plane; the vacuum cadmium, however, tended to branch into several cracks.

The microscopic details of the induced failures were essentially the same for low embrittlement cadmium and vacuum cadmium plate. Figures 24, 26, and 28 are fractographs taken on a low embrittlement cadmium sample. The fractographs were taken at 3-millimeter intervals, beginning at the cadmium steel interface and progressing into the steel. The same type series from a vacuum cadmium sample is presented in Figures 25, 27 and 29. The only apparent difference between the two can be seen in Figures 24 and 25. Adjacent to the cadmium-steel interface, the low embrittlement cadmium sample

(Figure 24) was comprised completely of cleavage fracture. The vacuum cadmium sample (Figure 25) consisted of a mixture of intergranular and cleavage fractures. Near the middle of the origins, the difference disappeared and the topography became mixed cleavage and intergranular cracking as demonstrated in Figures 26 and 27. The topography remained the same until the onset of catastrophic failure. Figures 28 and 29 show the fracture topography adjacent to the rapid fracture zone. In both cases, the rapid fracture zone was comprised of dimpled rupture as illustrated in Figure 30.

Results obtained using carbon replicas on the transmission electron microscope were the same as those obtained using the scanning electron microscope. Figures 31 through 34 depict the topography observed progressing into the steel from the cadmium-steel interface. The initial mode of propagation was a mixture of intergranular and cleavage cracking (Figures 31 to 33). The fast fracture was dimpled rupture as shown in Figure 34.

2. SERVICE FAILURE RESULTS

a. Introduction

Metallographic examination of the conditions found in the A-7 aircraft UHT shafts and horn failures encompassed low magnification and high magnification studies, which will be discussed separately in this section. The comparison between the induced cadmium failures shown in Section IV, paragraph 1 and the service failures will be made in Section IV, paragraph 2d

b. Light Microscopy

The photomicrographs in Figures 35 through 42 characterize the conditions found in the service failures of the UHT shafts and horn. Examination of all seven failures at the tapered pin hole-origin revealed no evidence of cracks parallel to the fracture surface. Figures 35, 37, 38 and 40 exhibit typical origins. Evidence of shear lips at the hole (Figures 35 and 41) indicates these failures initiated below the surface. In nearly all failures small intergranular cracks were associated with the immediate fracture surface in the intergranular nucleation area (Figures 38, 39, and 42). The larger perpendicular crack shown in Figure 36 occurred inboard from the tapered pin hole in the transition zone from intergranular to rapid fracture and was associated with the catastrophic failure. These cracks, which occurred in three of the seven failures, were a mixture of intergranular and transgranular modes.

Metallographic examination under polarized light gave very little information as to the presence of diffused cadmium. Due to irregularities of the fracture surface, on successive planes, getting a close bond of the mounting compound to the specimen was impossible. This left void areas which become traps for foreign material during polishing. For example, diamond paste and alumina polishing compounds examined under polarized light appear similar to cadmium. Also, while the specimen was being polished the soft cadmium was cut loose from the plated surface and was carried on the polishing wheels and entrapped in the void areas and sharp fracture profiles.

Metallographic examination and microhardness determinations revealed no abnormalities in the structure of the 4340 materials used in this investigation.

c. Electron Microscopy

The service failures, which include six UHT shafts and one UHT horn, were examined using carbon replicas on the transmission electron microscope. Also, for comparison purposes two of the UHT shafts were examined using the scanning electron microscope.

Figures 45 through 50 show the fracture origin and corresponding electron fractograph for each of the seven service failures. Note that in each case the fracture origin was located subsurface. Several cases existed (Figures 47, 49, 53, 55, and 57) in which the origin cracks propagated into the pin holes from the subsurface initiation point. Close examination is required to establish the subsurface initiation. In other cases, Figures 45 and 51, a small shear lip can be seen along the edge of the pin holes. This more clearly shows the subsurface nucleation, since the final ligament of the hole was sheared during the secondary fracture phase. In all cases the fracture topography consisted of intergranular cracking. The tell tale hairline crack indications typical of hydrogen embrittlement were present in all cases. Also small pockets of dimpled rupture were observed intermingled with the intergranular topography. Figures 61 through 65, the scanning electron micrographs, further illustrate and confirm the findings from use of the transmission electron micrograph.

An intensive search was made for evidence of corrosion attack, but no corrosion was found on any of the fracture surfaces.

The conclusion reached on service failures establishes hydrogen embrittlement as the culprit. However, there is some question as to the source of hydrogen. This is further confused when one considers the time of failure. Some of the parts failed soon after assembly, so the source of hydrogen could have been a processing step such as copper plating prior to heat treatment. Attempts to duplicate the embrittlement in the processing sequence have been unsuccessful, and the long time span between assembly and failure on most of the failed parts suggests a good possibility of environmental influence. The hydrogen may have entered the part during service as a product of cadmium corrosion, a possibility which is borne out by the higher frequency of failures when cadmium was intentionally applied in the holes.

d. Comparison of Cadmium Induced Failures and Service Failures

Low magnification microscopic examination of the induced failures and service failures indicate several perceptible differences. Figures 14 through 19 represent the induced failures and Figures 35 through 42 the

service failures. The noticeable microscopic features differ as summarized below:

Cadmium Induced Failures	Service Failures
Failures were surface initiated (no shear lips).	Failures were subsurface initiated (shear lips, Figure 35).
Cracks in the initiation area were both intergranular and transgranular modes.	Cracks in the initiation area were of an intergranular mode.
Cracking parallel to the fracture planes were observed (Figures 16 and 17).	No cracking parallel to the fracture planes was observed.

Corroborative information is shown in the electron fractrography discussion in the next paragraph.

Comparison of fractographs from the embrittled samples (Figures 31 through 33), with service failure fractographs (Figures 43 through 58), reveals a striking difference. The induced failures exhibited significant areas of cleavage intermingled with the intergranular cracking. Such was not the case with the service failures; instead, the service failures were comprised predominantly of intergranular fracture within the origin area. This same result was evident from scanning electron microscope results. Note that in Figures 60 through 65 taken from service failures A7B-137 and A7D-8 the fracture topography consisted of intergranular cracking mixed with pockets of dimpled rupture. Hairline crack indications on the facets of the grains were evident in all of the fractographs. Comparing these with Figures 20 through 29 taken from the embrittled test samples, several differences were noted. The embrittled samples consisted of intergranular cracking mixed with large areas of cleavage rather than small dimpled rupture areas as with the service parts. Also, there was a conspicuous lack of hairline crack indications on the embrittled samples. Another feature which was quite evident was that the transition from intergranular cracking to the dimpled rupture of the fast fracture zone was very abrupt in the embrittled samples. This transition was very indistinct in the service parts however. Comparison of Figure 21 with Figure 60 shows the most significant difference between the two types of failure. Note that the origin of cracking in Figure 21 and embrittled specimen lies at the surface. However, in Figure 60, a service failure, the original cracking occurred beneath the surface. This fact was demonstrated plainly by the existance of a shear lip along the surface at the pin hole. Thus it was apparent that the test specimens initiated failure from the surface whereas the service failures initiated subsurface.

3. ELECTRON MICROPROBE STUDIES

a. Induced Cadmium Embrittled Fractures

(1) ARL Probe Results

Figure 66 shows the origin of this fracture in the backscattered electron mode. Figures 67 and 68 show the same area in the secondary electron and specimen current modes respectively. Although each gives generally the same picture of the fracture surface, certain advantages can be gained from examining the various modes. For example, the secondary electron image in Figure 67 perhaps gives the clearest idea of surface topography. Figure 68, the specimen current image, gives an indication of atomic number variation on the surface. Figure 66 is roughly the negative image of Figure 68, in that the two effects reflect opposite behavior of electrons on interacting with matter.

Figure 69 is a cadmium distribution map of the same area. Figure 70 shows the cadmium concentration profile along this surface measured while moving the electron beam down the hatched vertical line in the center of the previous photographs. Both indicate there is some cadmium on the fracture surface, but they do not indicate any concentration gradient from the edge inward. However, cadmium point counts, shown plotted in Figure 71 show that such a gradient is present.

(2) CAMECA Probe Results

Figure 72 is the backscattered and secondary electron scan of a portion of the origin of the same induced cadmium-embrittled failure. Figure 73 shows cadmium distribution over the same surface area. That the dark irregular area near the upper right corner of Figure 72 is the cadmium plate is clearly revealed in Figure 73. In addition, a gradient in cadmium concentration can be seen, decreasing with distance from the plate inward. This gradient is confirmed by the plot of point counts, with distance moved inward from the plated edge shown as Figure 74.

Clearly the two probes give equivalent results on this sample area.

b. Service Fractures

(1) Shaft from A7B-121

(a) ARL Probe Results

Figure 75 shows the backscattered electron image at the fracture origin. The light-colored areas near the edge appear to be the cadmium plate. This is confirmed by the cadmium distribution map in Figure 76 and the concentration profile, Figure 77.

Here again, no concentration gradient is evident from the plate inward. The plot of cadmium x-ray point counts along the same line, beginning at the

sample edge shown in Figure 78, confirms this. Cadmium concentration drops off abruptly on leaving the plate, with no appreciable gradient.

(b) CAMECA Probe Results

Figure 79 shows the backscattered and secondary electron image of the A7B-121 fracture origin. The cadmium distribution map, shown in Figure 80, indicates scattered pockets of cadmium distributed over the fracture surface. There is no evidence of a concentration gradient, however. Point counts for this area are shown in Figure 81. No gradient is present. The count rate is sporadic, but uniformly low.

Because results reported to this point indicate essentially complete agreement between the two microprobes, only the results obtained on one of the instruments are reported for the remaining fractures.

(2) Shaft from A7B-107 (Service No. 0070)

Figure 82 shows the backscattered electron image for this fracture origin. Toward the top of this photograph the cadmium-plated inner surface of the pin hole drops away from the plane of focus. The remainder of the photograph shows the topology of the fracture surface, with several dark, roughly circular spots near the bottom center.

Figure 83 shows cadmium distribution over the same area. Cadmium can be seen at the top of this picture on the plated surface and in pockets near the bottom, corresponding roughly to the dark spots in Figure 82. Apparently some cadmium has been mechanically smeared into low spots on the fracture surface, probably during handling of the parts. There is no indication, however, of a concentration gradient from the edge inward. The lack of such a gradient was confirmed by point counts.

Figure 84 shows the cadmium profile down the centerline of Figure 82. This again indicates no concentration gradient, in agreement with Figure 83 and the corresponding step scan.

(3) Shaft from A7B-137

Figures 85, 86, and 87 show, respectively, for this sample the backscattered electrons, cadmium distribution, and cadmium profile. Again, cadmium is apparent on the plated surface, but no gradient is seen on the fracture surface itself. And again, the step scan analysis indicated no gradient on the fracture surface.

(4) Shaft from A7B-183

Figures 88, 89, and 90 show backscattered electrons, cadmium distribution, and the cadmium profile. Results are in agreement with those reported for the above sample.

(5) Shaft from A7D-8

Figures 91, 92, and 93 show similar results for this in-service fracture.

(6) Shaft from A7B-181

Figure 94 shows the backscattered electron image for the origin of this fracture. For comparative purposes, the secondary electron image is shown in Figure 95 and the specimen current image in Figure 96 for the same surface area. These furnish a good example of the strong points in each of the three types of presentation. The backscattered image emphasizes the system of deep cracks associated with this fracture origin. The secondary image gives a good general picture of surface topology, while the specimen current image hints at elemental segregation on various parts of the surface area under consideration.

Figures 97 and 98 show cadmium distribution and distribution profile respectively for this specimen. Again, cadmium can be seen on the plated surface at the top of the photo, but no gradient appears on the fracture surface. Again, step scan analysis agreed with the observed lack of a cadmium gradient.

(7) Horn from A7B-183

Figure 99 shows the backscattered electron image of the origin of the fractured UHT horn from A7B-183. Corresponding cadmium distribution and profile for this fracture area are shown in Figures 100 and 101. As on the shaft failures, no cadmium gradient was found.

4. MECHANICAL PROPERTY TEST RESULTS

The mechanical properties and hardness readings on the embrittled specimens and service failures where sufficient material was available for tensile testing are shown in Table II.

The embrittled test samples all failed without yielding. The control samples exhibited normal mechanical properties. The slightly lower strength exhibited by the low-embrittlement cadmium samples can be attributed to the greater depth of the cadmium cracking in those samples.

The service parts surpass the required mechanical properties. However, it should be noted that in every case the strength level and hardness was on the high side of the range. The tensile properties and hardness of the horn were above the drawing requirements range.

5. AUGER ELECTRON SPECTROSCOPY

Figure 102 shows the Auger Electron Spectrum obtained on the induced cadmium-embrittled fracture. Visible on the spectrum are the gold plate, sodium and chlorine from the salt crystal used as mask, carbon (probably

TABLE II

MECHANICAL PROPERTIES

Specimen No.		Fty, psi	Ftu, psi	% Elong. (in 1 in.)	R/A, %	Hardness, Rockwell C
Low Embrittlement Cadmium						
	1	---	267,100	---	---	52
	2	---	269,600	---	---	52
Vacuum Cadmium						
	1	---	279,500	---	---	52
	2	---	280,700	---	---	52
Control	3	209,700	275,900	16.0	46.5	52
Control	4	209,400	276,500	14.0	44.4	52
		From A7D-8 (Shaft)				
	1	210,000	289,000	9.0		53-54
	2	213,000	291,100	9.0		53-54
	3	206,700	288,900	9.0		53
		From A7B-181 (Shaft)				
	1	219,000	290,000	8.0		53-54
	2	223,100	291,400	8.0		54
		From A7B-183 (Shaft)				
	1	221,500	288,400	8.0		53-54
	2	218,700	288,400	9.0		53
		From A7B-137 (Shaft)				
	1	242,300	294,300	8.0		53-54
	2	243,400	294,200	9.0		53-54
		From A7B-183 (Horn)				
	1	227,700	239,800	7.0		47-49
	2	234,000	246,600	8.0		48-49
	*	217,000	260,000	6.0		50-53
	**	180,000	200,000	---		43-46

* Minimum mechanical properties required for the shafts.
** Minimum mechanical properties required for the horns.

deposited during microprobe analysis), oxygen, and iron from the steel substrate. Prominent in the spectrum are the several peaks between 300 and 400 eV due to cadmium on the surface.

By contrast, the Auger spectrum of the in-service fracture surface is shown in Figure 103. Here the gold peaks are less prominent, indicating better positioning of the beam in the window. Carbon and iron are more prominent, as is oxygen. The chlorine peak is present, although sodium is doubtful. Cadmium is present, but at a significantly lower level than on the induced fracture. This probably reflects the presence of the small pockets of cadmium previously observed on several of the fracture surfaces during the microprobe investigation. This small amount of cadmium was apparently mechanically abraded from the plated surfaces onto the fracture surfaces during the storage since these failures were originally examined.

SECTION IV

CONCLUSIONS AND RECOMMENDATIONS

The objectives of this program were met, and the following is concluded.

1. Solid cadmium embrittlement was not the failure mode on any of the A-7 aircraft failed shafts and horn. (See Table III.)

2. Hydrogen embrittlement was established as the failure mode.

3. The characteristics of solid cadmium embrittlement were defined, and the differences in this failure mode and hydrogen embrittlement can be established by laboratory means.

4. Service history indicates that hydrogen embrittlement cracking will occur in 260 Ksi UTS 4340 steel at lower stress levels than solid cadmium embrittlement will occur, at ambient aircraft temperatures where moisture is present.

5. It is recommended that caution be exercised wherever high strength steel structural parts are heavily loaded and in intimate contact with cadmium. Also, this work suggests three areas for further research:

- Develop protective systems other than cadmium for highly stressed high strength structural parts to be used in a hostile environment.

- Investigate the mechanism of embrittlement, to establish the authenticity of the cadmium corrosion theory or pinpoint other factors affecting this type of failure.

- Establish environmental hydrogen embrittlement threshold values for high strength steels that have been protected by various systems.

TABLE III

SUMMARY OF SOLID CADMIUM EMBRITTLEMENT AND SERVICE FAILURE FINDINGS

TEST METHOD	OBSERVATIONS	
	CADMIUM INDUCED FAILURES	SERVICE FAILURES
Low Magnification	Surface initiation Intergranular and transgranular modes Cracks parallel to fracture planes	Subsurface initiation Intergranular modes No cracks parallel to fracture planes
High Magnification	Intergranular cracking with areas of cleavage No evidence of hairline cracks on grain facets Surface initiation	Intergranular cracking, with areas of dimpled rupture Hairline cracks on grain facets Subsurface initiation (shear lip)
Electron Microprobe	Cadmium gradient from surface inward	No cadmium gradient
Auger Spectroscopy	Significant cadmium on the fracture surface	Low level of cadmium on the fracture surface
Mechanical Properties	No ductility	Evidence of ductility

BIBLIOGRAPHY

A. Fager, D. N. and W. T. Spurr, "Solid Cadmium Embrittlement: Titanium Alloys," Corrosion 26, 409 (1970) October.

B. Fager, D. N. and W. T. Spurr, "Solid Cadmium Embrittlement: Steel Alloy," Corrosion 27-72 (1971) February.

C. Shaffer, I. S. and J. A. Hoffner, "Investigation of Solid Cadmium Embrittlement in A-7 Horizontal Tail Actuator Horn and Shaft Assemblies," Department of the Navy,Report No. NADC-MA-7129 dated 4 June 1971

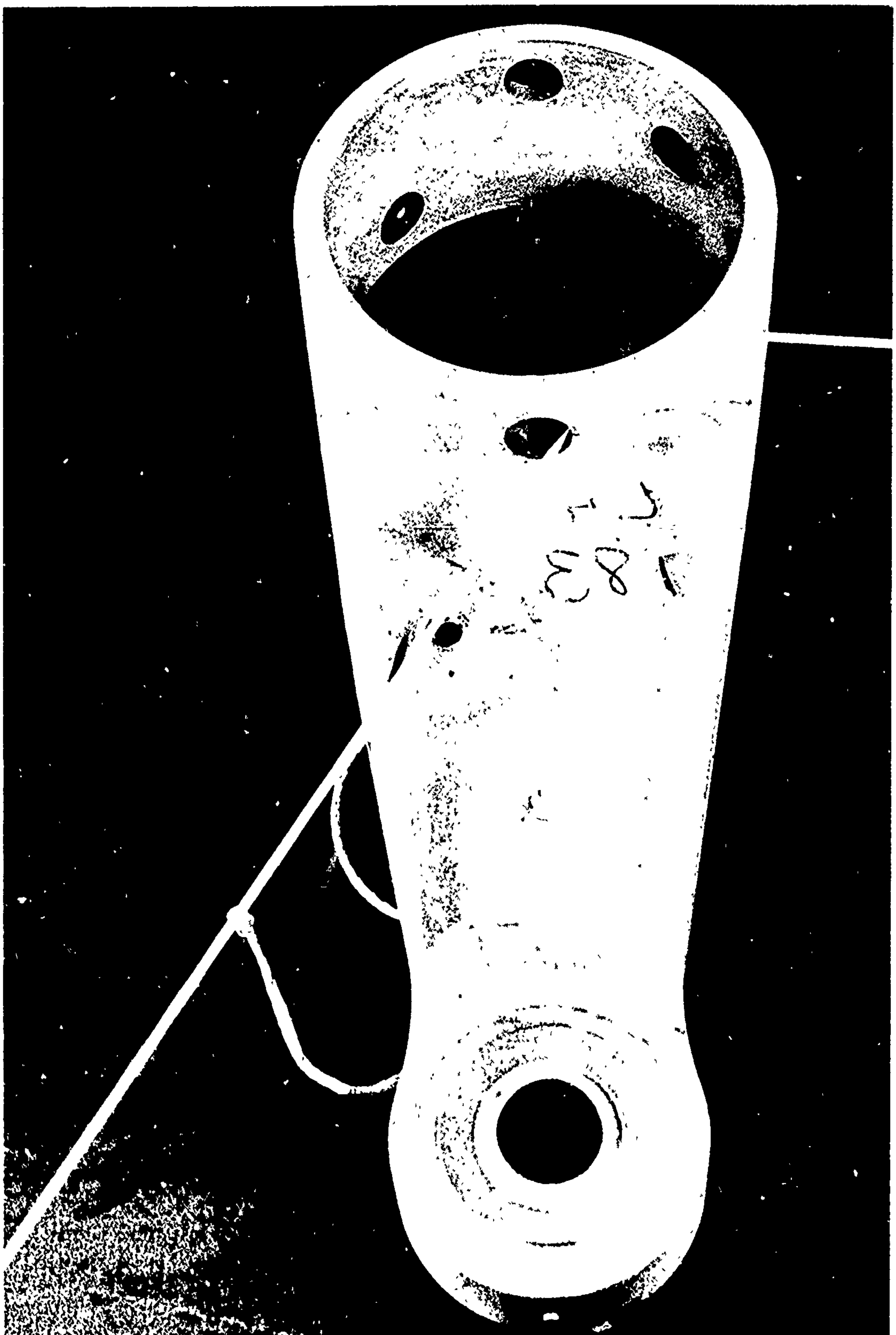

Figure 1. A-7 Horn P/N 15-160059

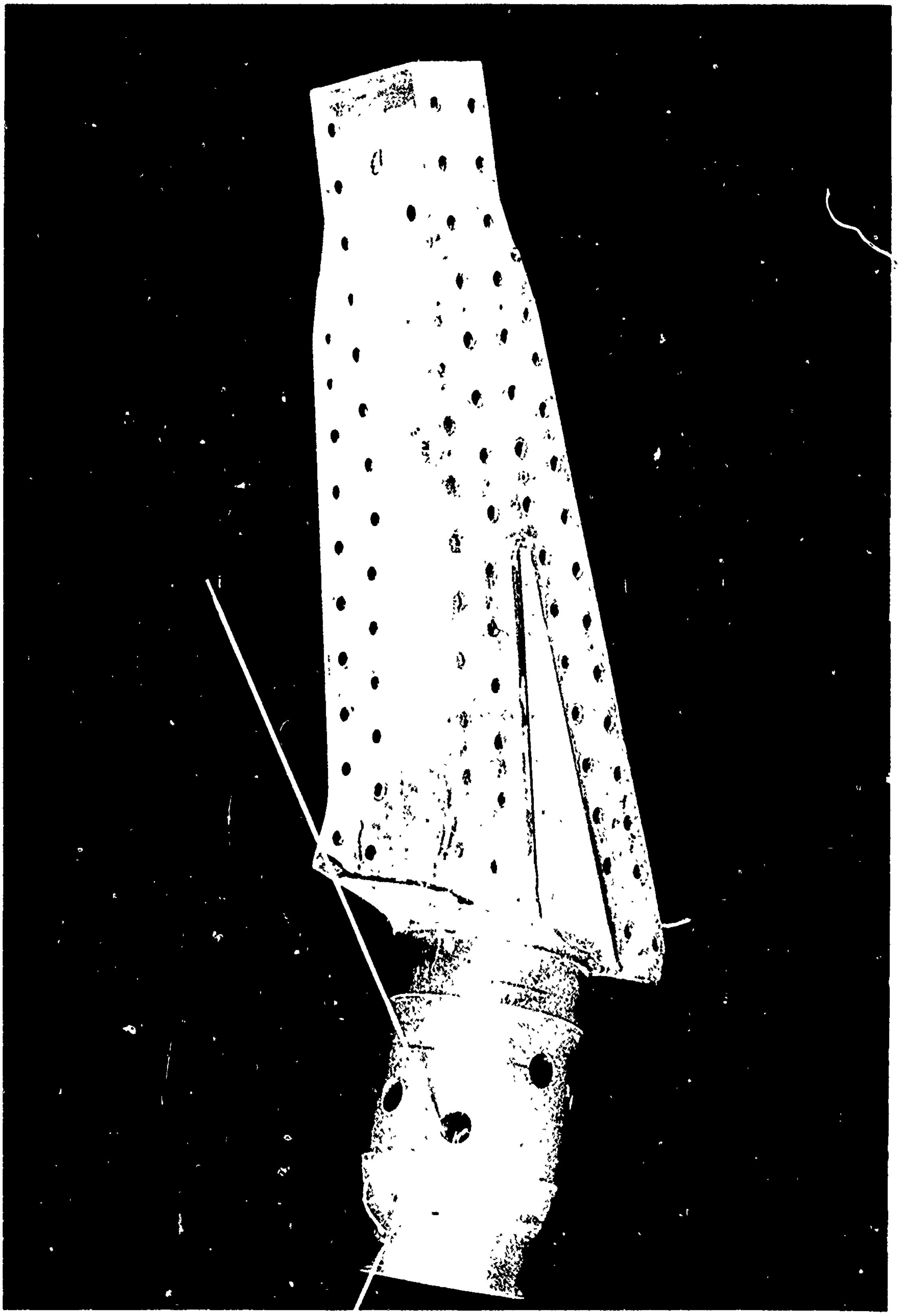

Figure 2. A-7 Shaft P/N 15-160003

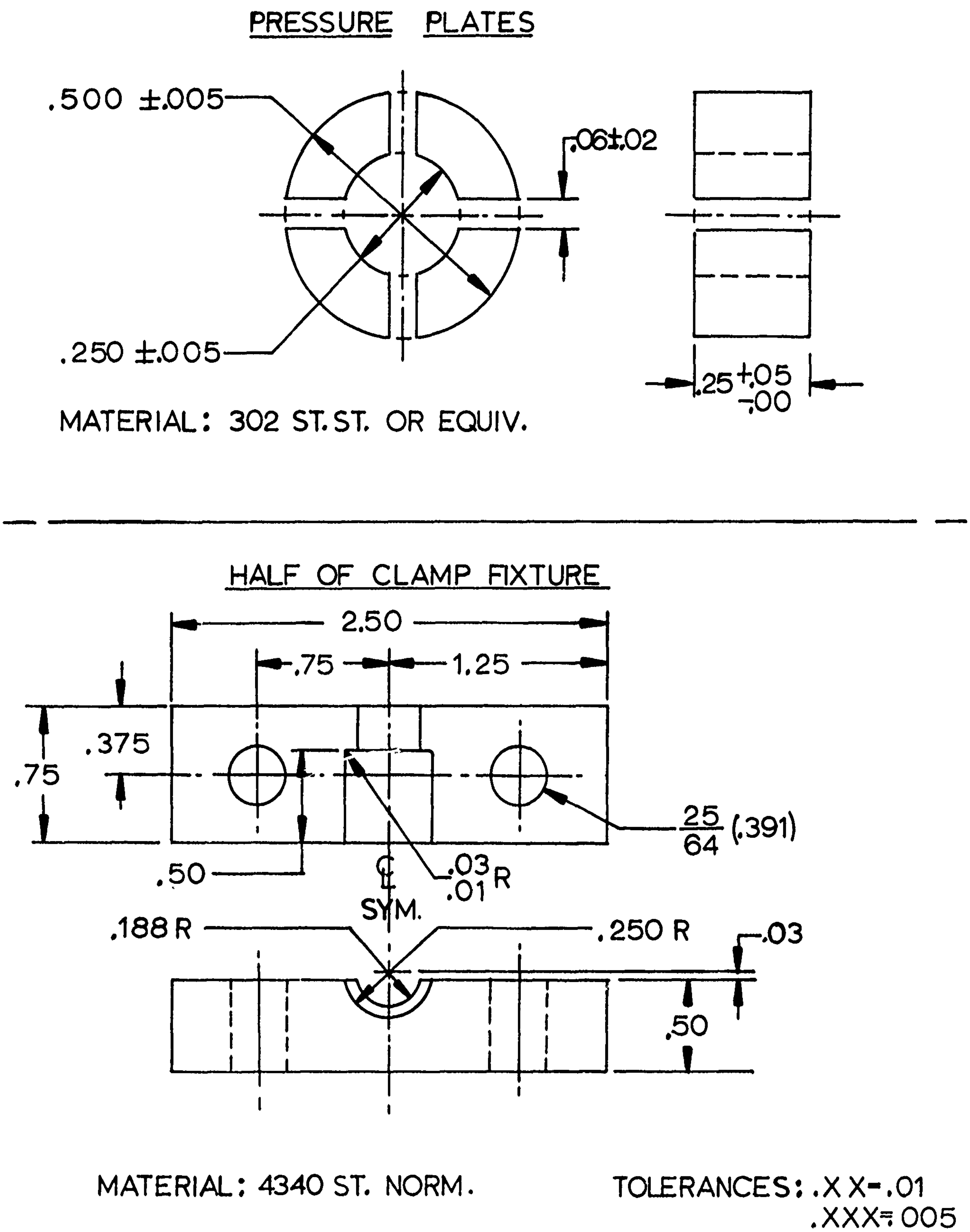

Figure 3 Pressure Plates and Half Clamp Fixture

"A" DIA AFTER PLTG +.003 −.000	TAPER PIN DWG. NO.(REF)
.674 63	CV15−160513−6
.689 63	CV15−160513−7
.704 63	CV15−160513−8

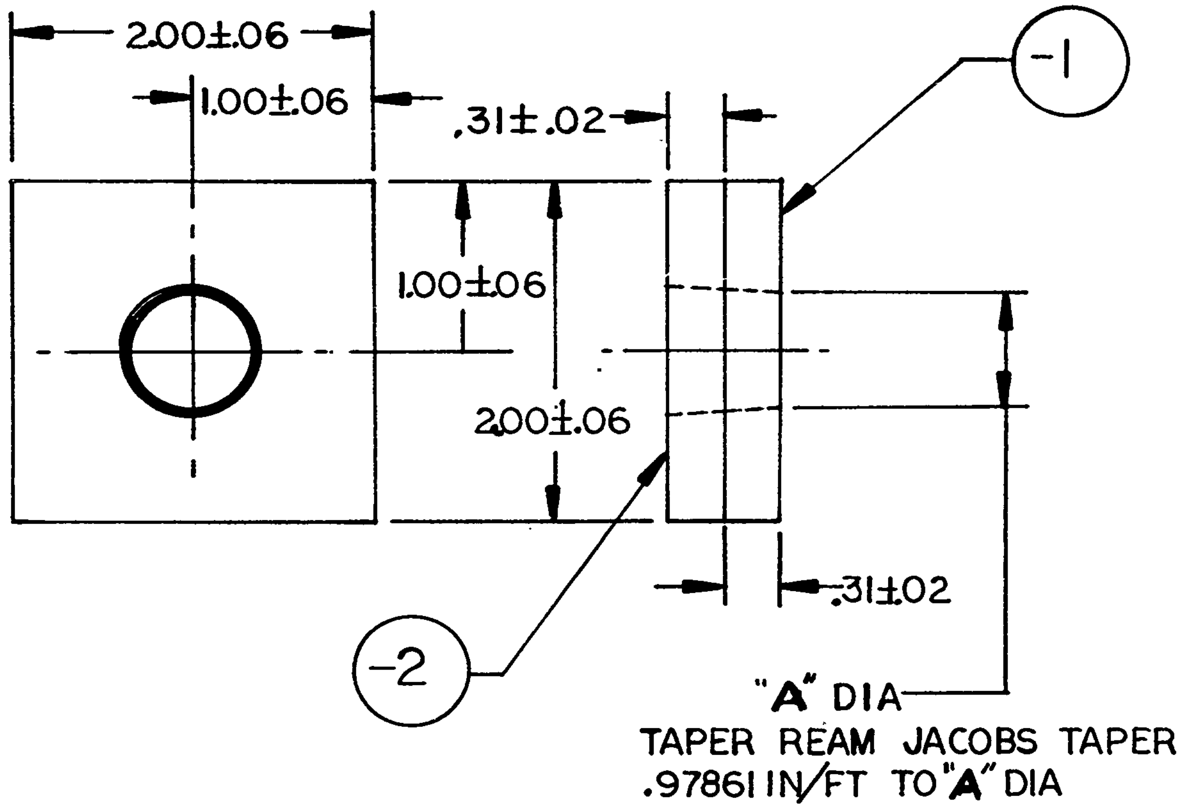

−2	PLATE	2X3X.5	4340 STL RECT BAR (COND C1) CVA1-585	ROCKWELL C43-46 (200,000 PSI MIN TS) CVA1-372	CAD PLATE .003−.005
−1	PLATE	2X3X.5	4340 STL RECT BAR (COND C1) CVA1-585	ROCKWELL C50-53 (260000 PSI MIN TS) CVA1-372	CAD PLATE .003−.005
PART NO.	NAME	STOCK SIZE	MATL & SPEC	HEAT TREAT	FINISH

Figure 4 Simulated A-7 Shaft and Horn Assembly

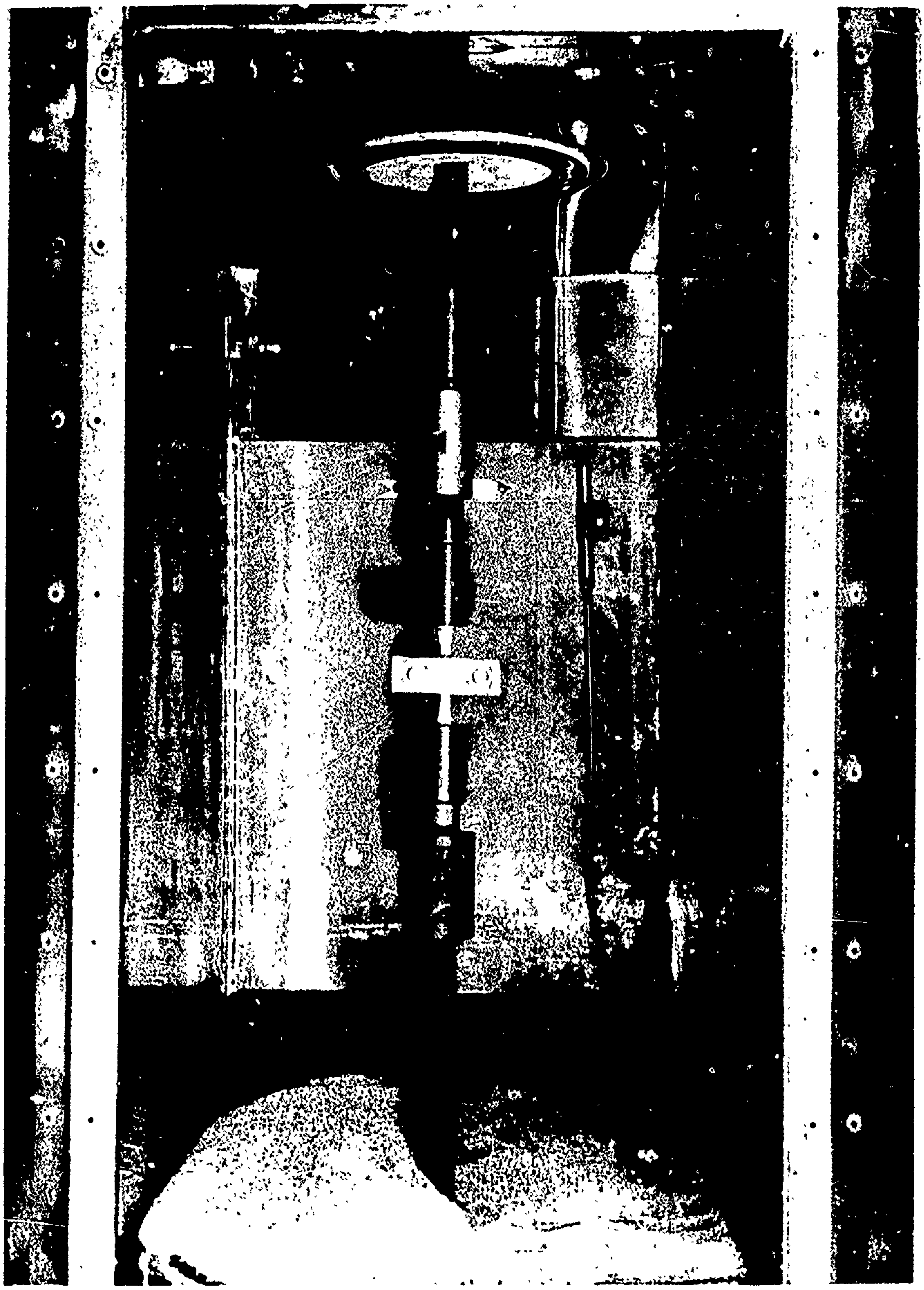

Figure 5. Cadmium Induced Embrittlement Test Fixture

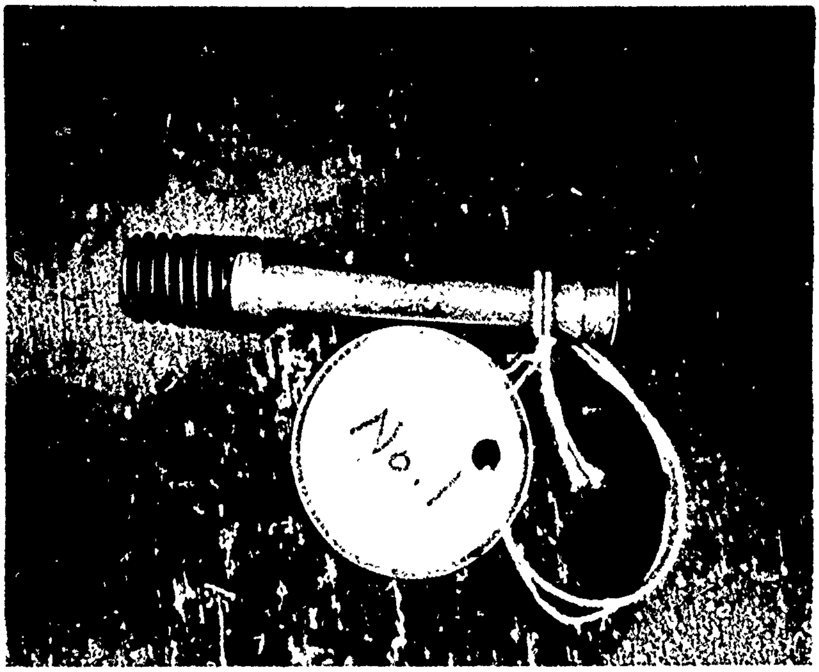

Figure 6. Embrittlement Test Specimen after Exposure for 20 Hours

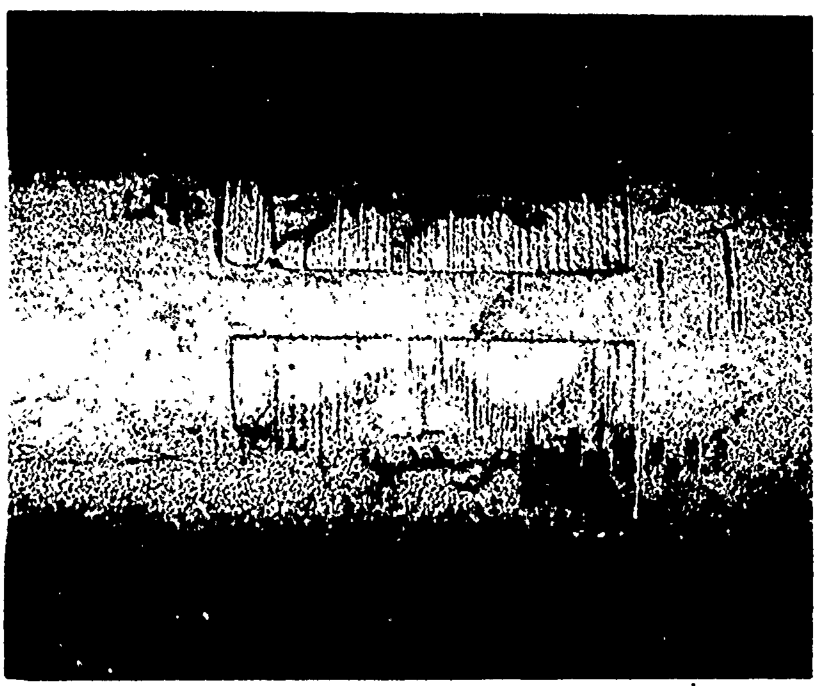

Figure 7. Close-Up View of Indentations Left by the Pressure Fixture

Figure 8. Comparison of Embrittled (Upper) Vs. Control (Lower) Specimens Showing Variation in Ductility at Fracture

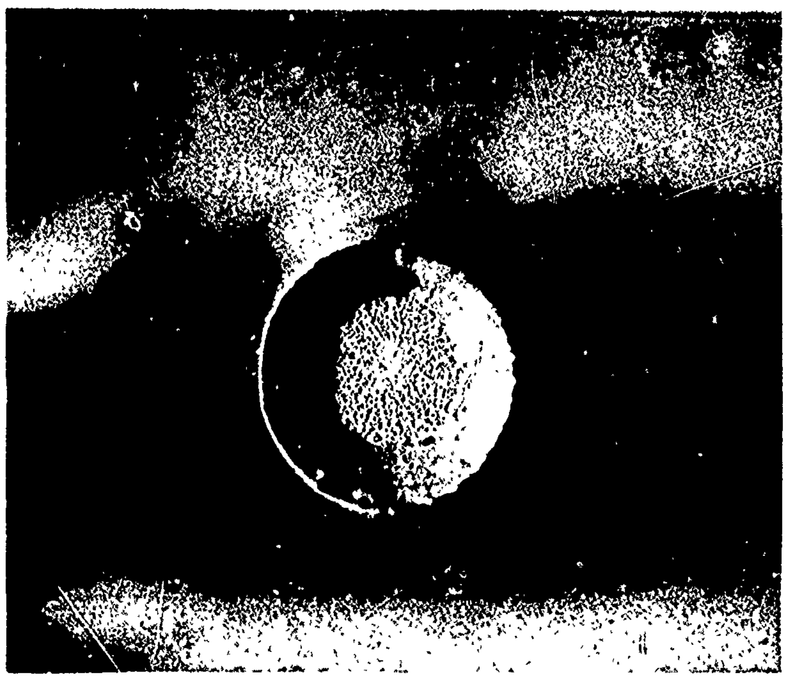

Figure 9. Fracture Surface on a Control Specimen Consisting of Normal Cup and Cone Fracture

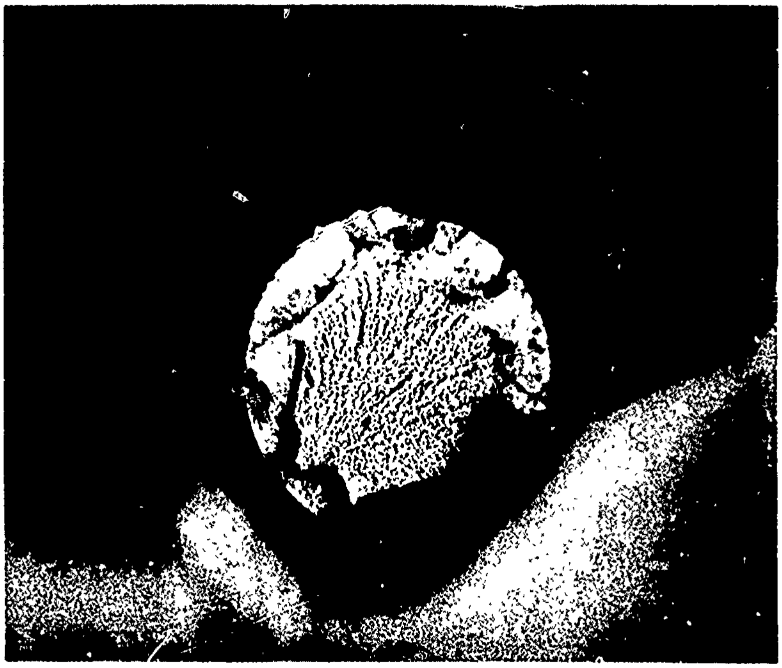

Figure 10. Fracture Surface of Ti-Cad Specimen No. 1.

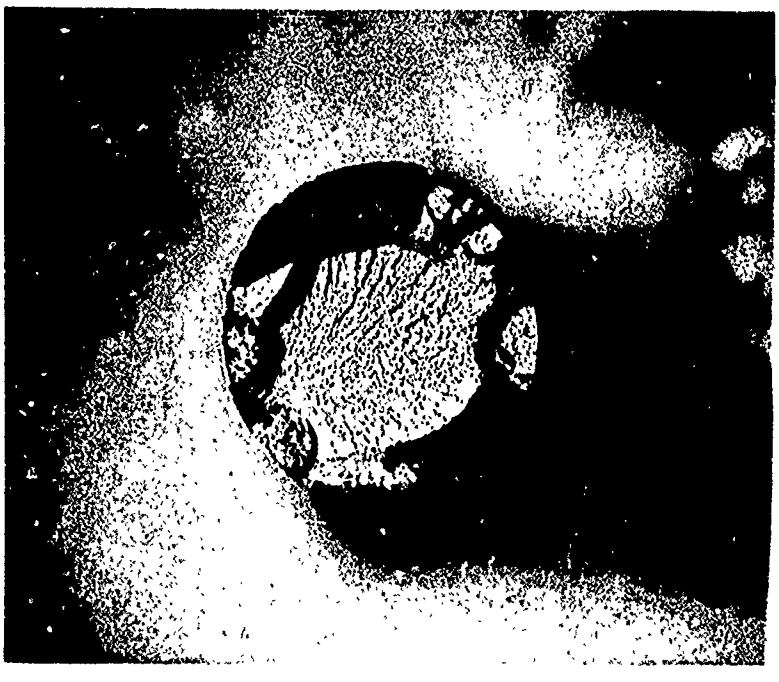

Figure 11. Fracture Surface of Ti-Cad Specimen No. 2.

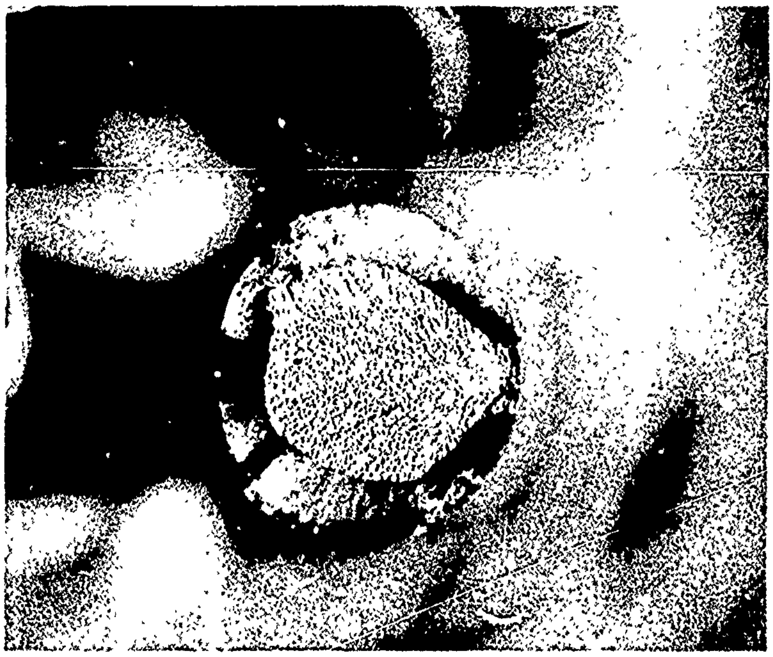

Figure 12. Fracture Surface of Vac-Cad Specimen No. 1.

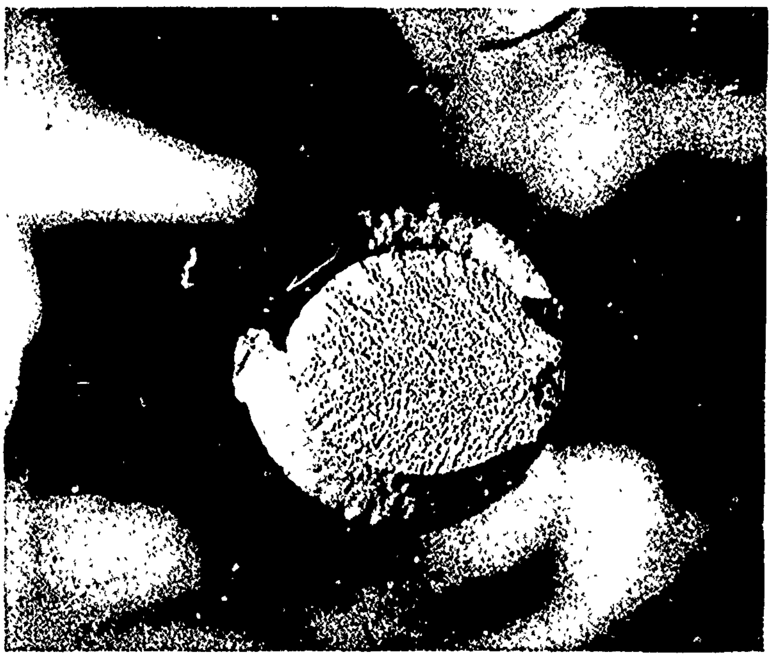

Figure 13. Fracture Surface of Vac-Cad Specimen No. 2.

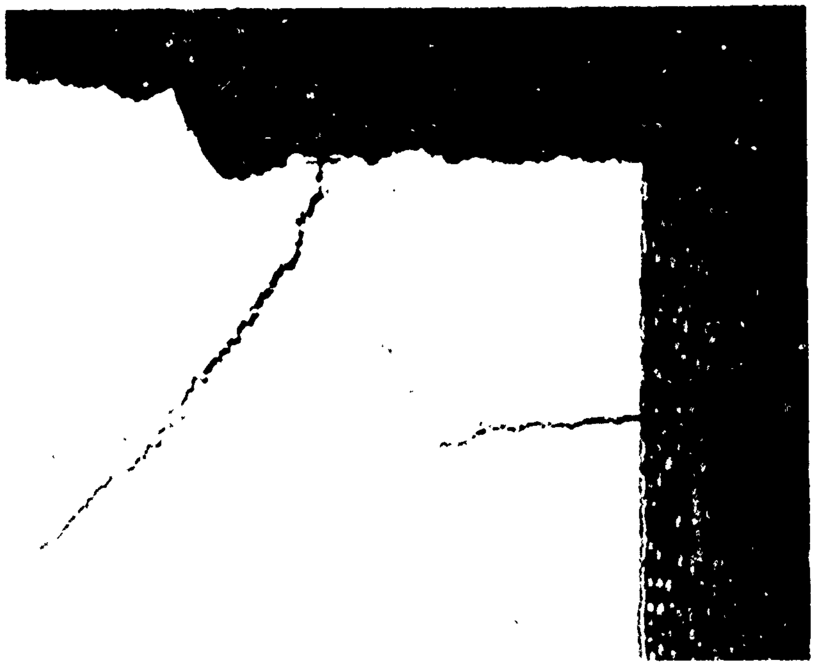

Figure 14. Photomicrograph of Cross Section of Ti-CD Induced Failure Exhibiting Cracks Perpendicular and Parallel to Fracture Origin at Top-right. Unetched

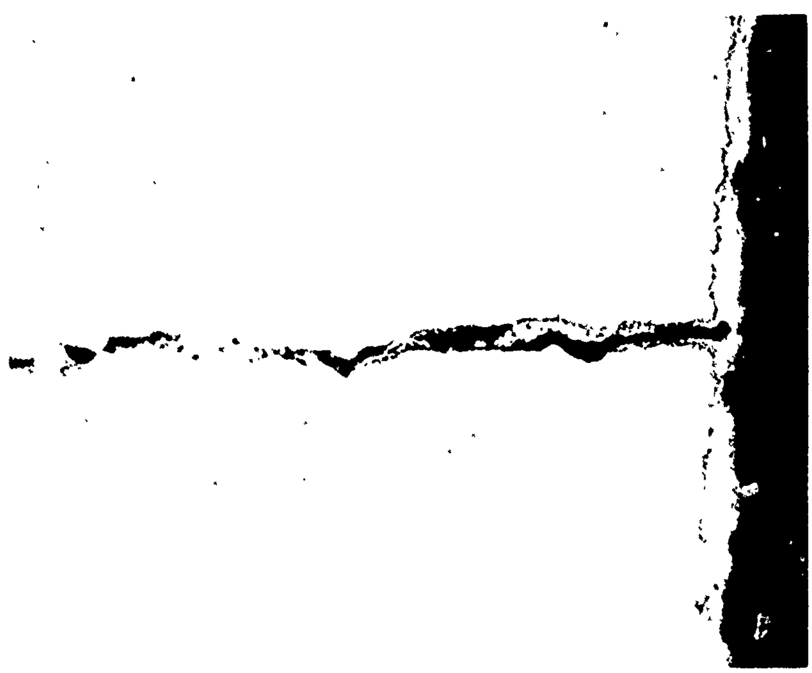

Figure 15. Parallel Crack Depicted in Figure 12 Showing Ti-CD Plate at Surface and Smeared into the Crack

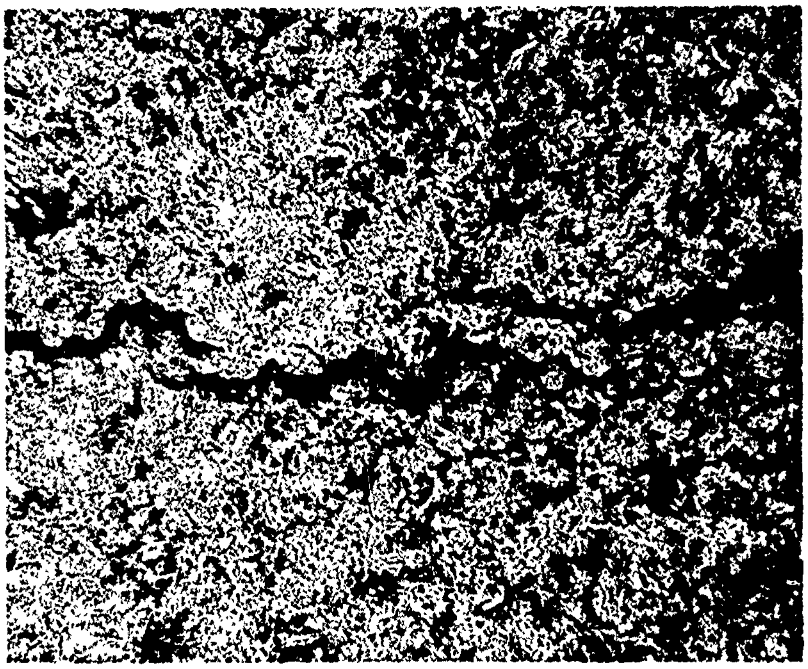

Figure 16. Perpendicular Crack Depicted in Figure 14 Showing Predominantly Intragranular Mode with Possible Cleavage.

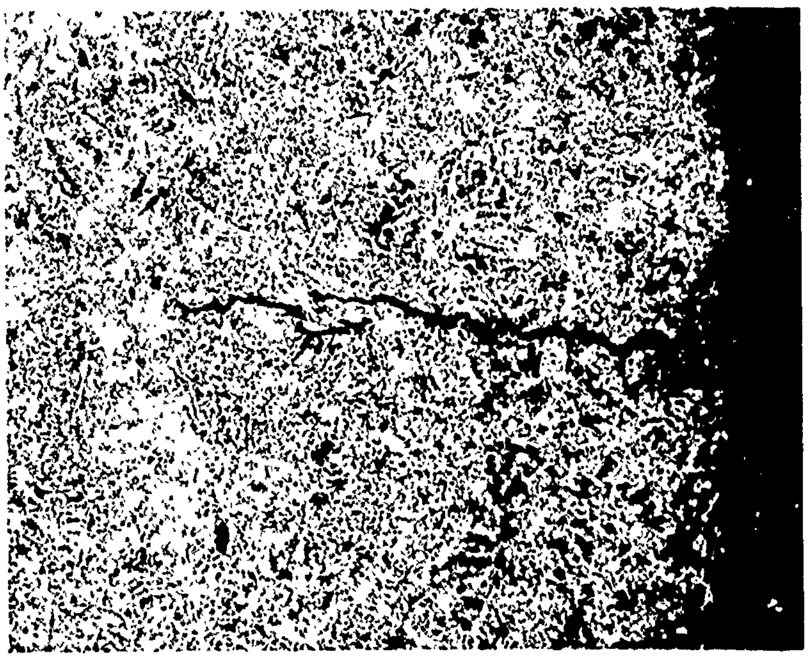

Figure 17. Additional Crack Parallel to Origin in Figure 14. Crack Initiated at the CD-Steel Interface and Appeared to be Both Intergranular and Cleavage Modes.

Figure 18. Cross Section of Vac-Cad Induced Failure Showing Origin at Top Right and Some Intragranular Cracking at the Fracture Surface. Unetched.

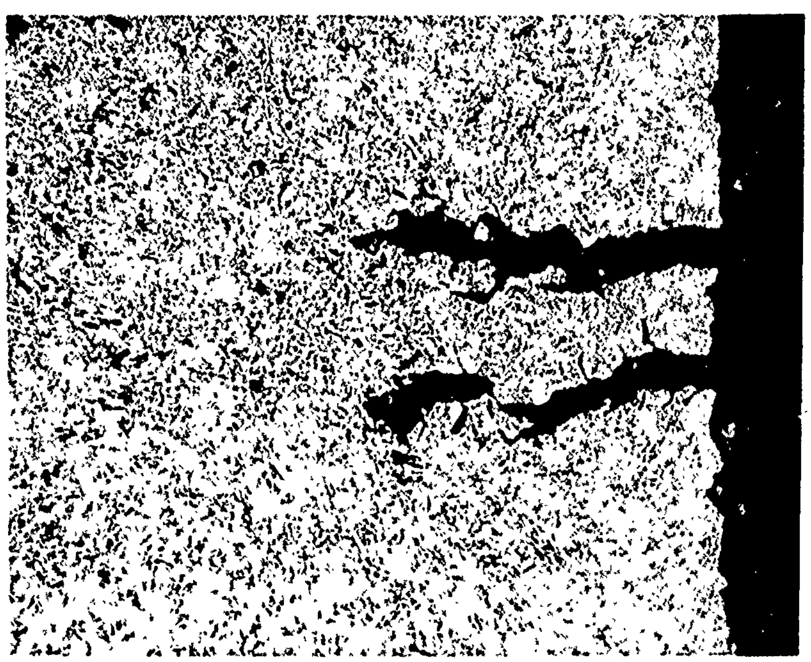

Figure 19. Parallel Cracks Adjacent to Origin in Figure 18. Intergranular Branching Can Be Seen Propagating from Cracks Opened Up During Tensile Loading. Nital Etch.

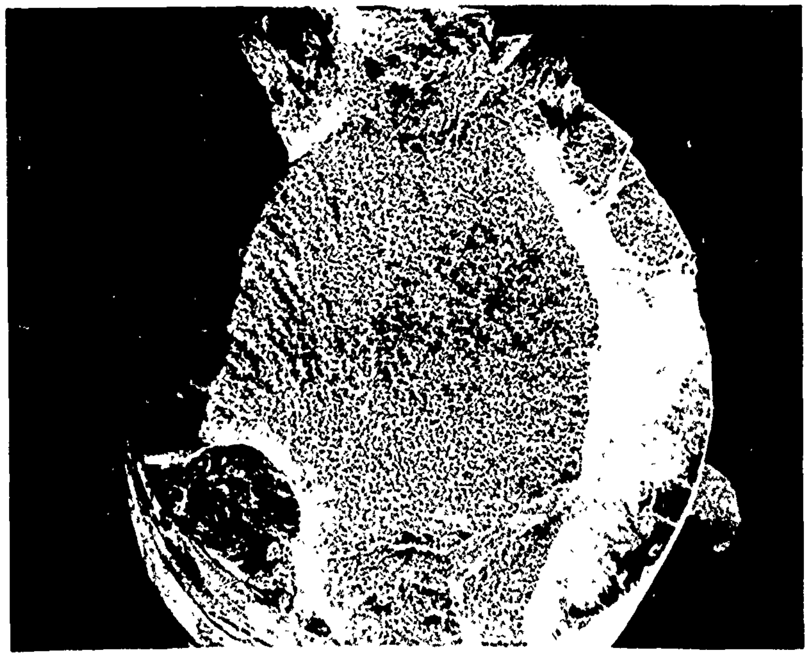

Figure 20. Photomicrograph Showing the Fracture Surface of Ti-Cad Specimen No. 2 - Scanning Electron Micrograph

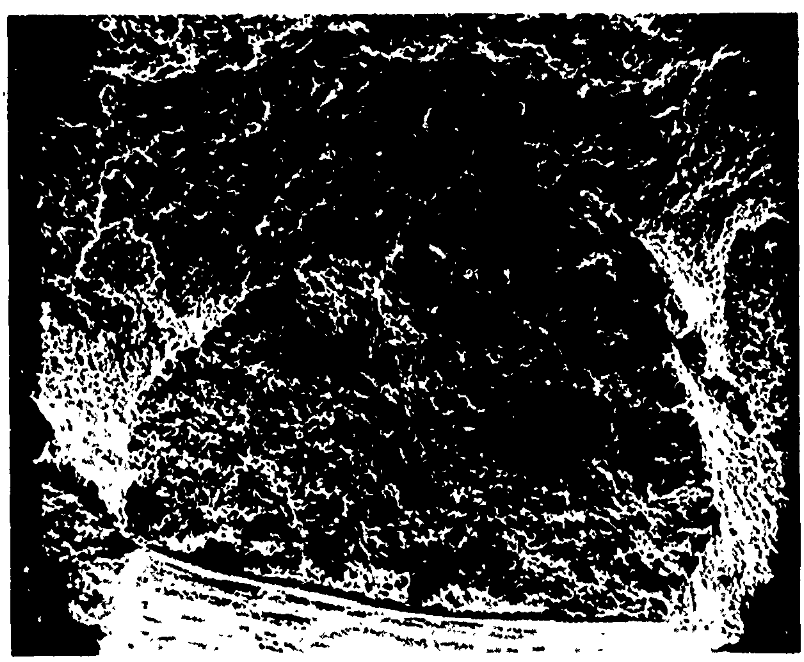

Figure 21. Photomicrograph Showing Details of One of the Origin Cracks on Ti-Cad Specimen No. 2 - Scanning Electron Micrograph

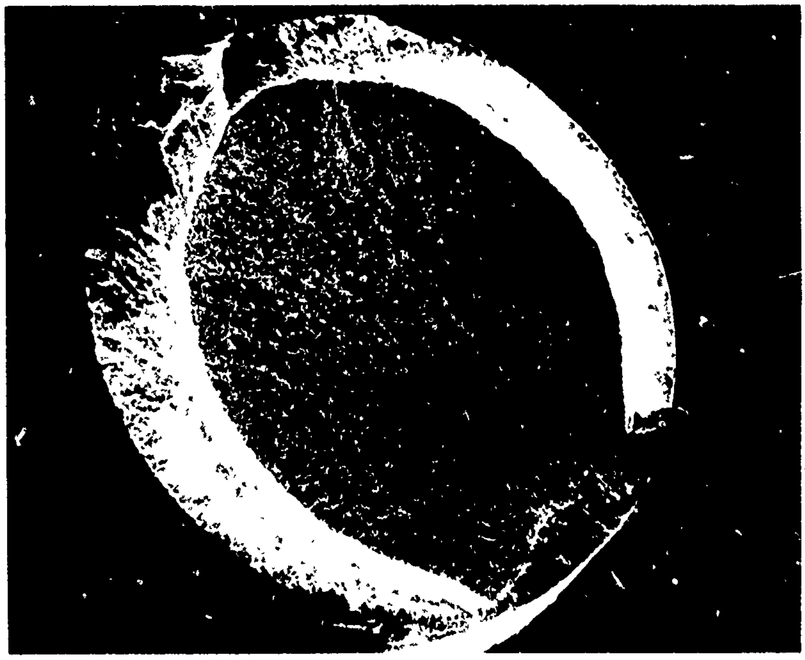

Figure 22. Photomicrograph Showing the Fracture Surface of Vac-Cad Specimen No. 2 - Scanning Electron Micrograph

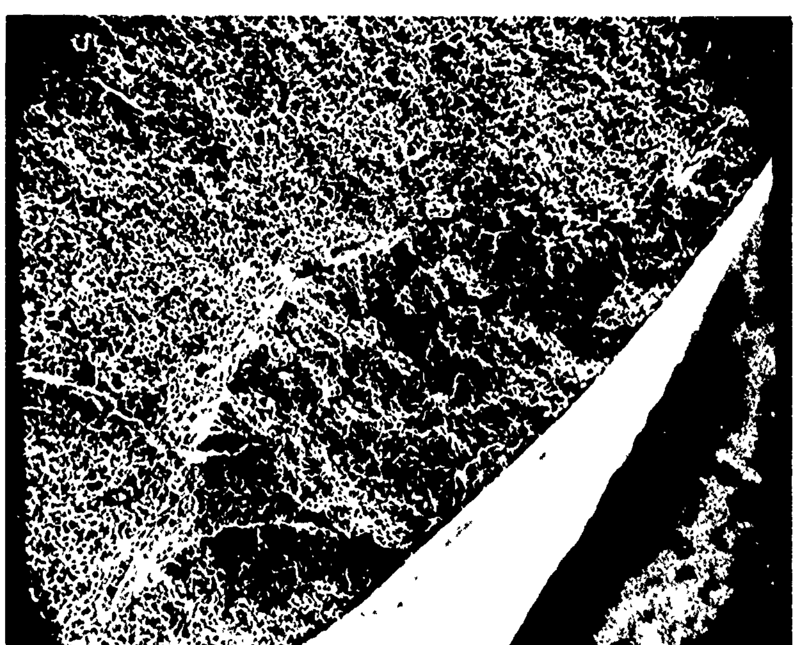

Figure 23. Photomicrograph Showing the Origin Crack of Vac-Cad Specimen No. 2 - Scanning Electron Micrograph

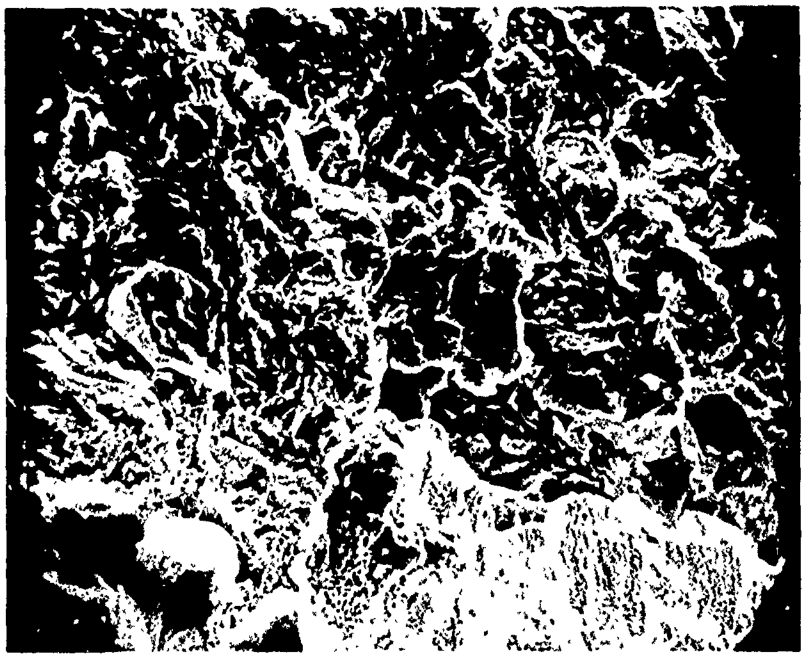

Figure 24. Fracture Topography Adjacent to the Cadmium Plate (lowermost) on Ti-Cad Specimen No. 2 - Scanning Electron Micrograph

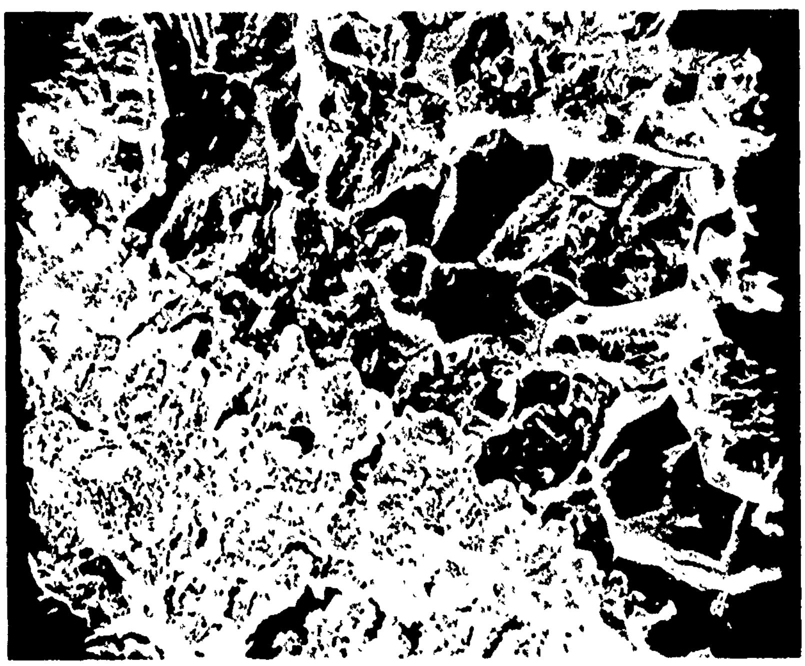

Figure 25. Fracture Topography Adjacent to the Cadmium Plate (lower left) on Vac-Cad Specimen No. 2 - Scanning Electron Micrograph

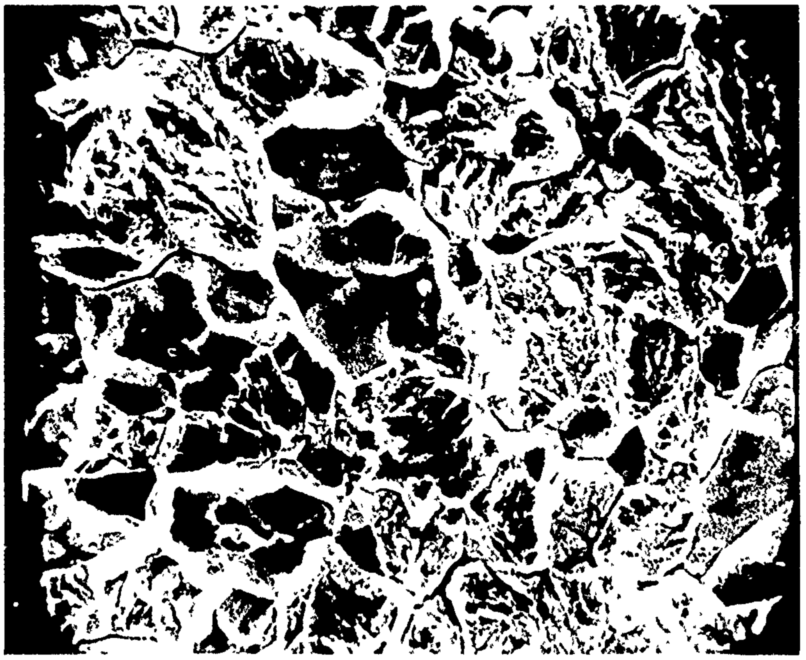

Figure 26. Fracture Appearance Near Mid-origin on Ti-Cad Specimen No. 2 - Scanning Electron Micrographs

Figure 27. Fracture Appearance Near Mid-origin on Vac-Cad Specimen No. 2- Scanning Electron Micrograph

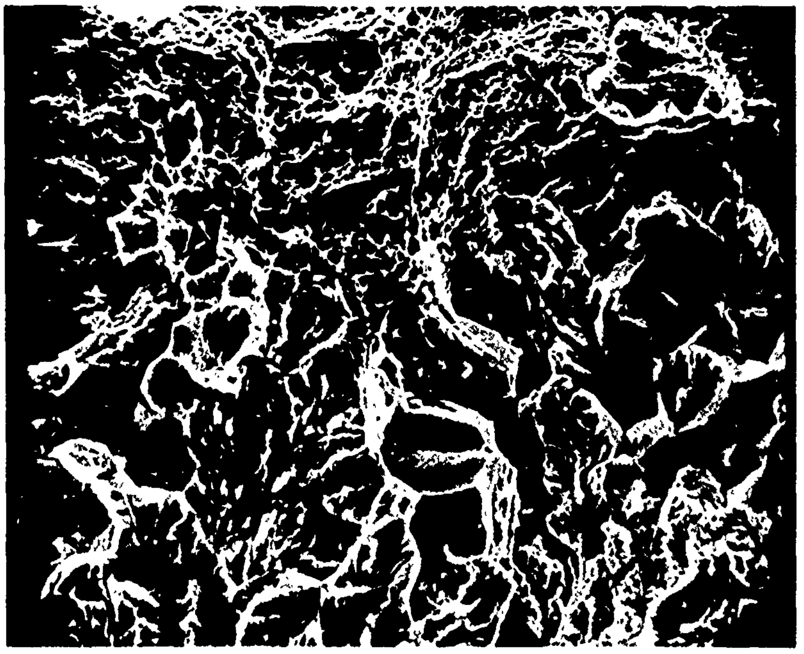

Figure 28. Fracture Appearance at the Onset of Fast Fracture in Ti-Cad Specimen No. 2 - Scanning Electron Micrograph

Figure 29. Fracture Appearance at the Onset of Rapid Fracture in Vac-Cad Specimen No. 2. Scanning Electron Micrograph

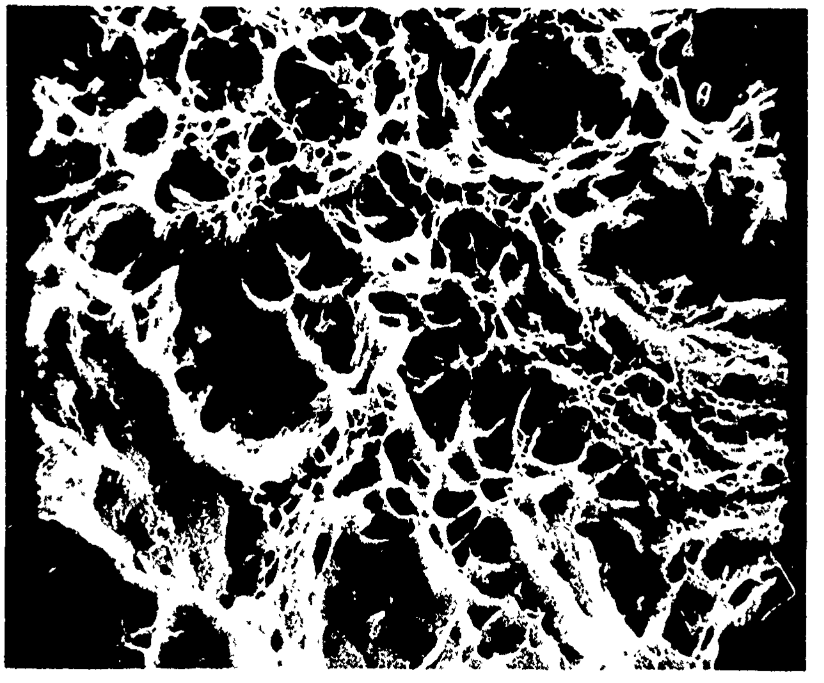

Figure 30. Appearance of the Fracture in the Rapid, Fracture Zone of the Embrittlement Test Specimens, Scanning Electron Micrograph

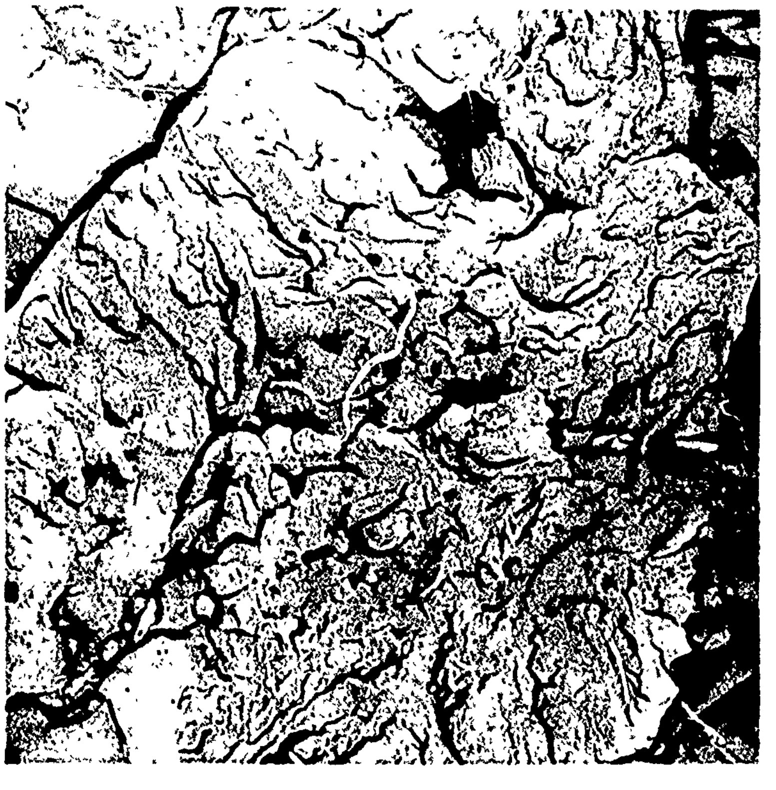

Figure 31. Fracture Appearance Near the Cadmium Plate on Ti-Cad Specimen No. 1. Transmission Electron Micrograph.

Figure 32. Fracture Appearance Near Mid-origin on Ti-Cad Specimen No. 1. Transmission Electron Micrograph

Figure 33. Fracture Appearance Near the Onset of Fast Fracture on Ti-Cad Sample No. 1. Transmission Electron Micrograph

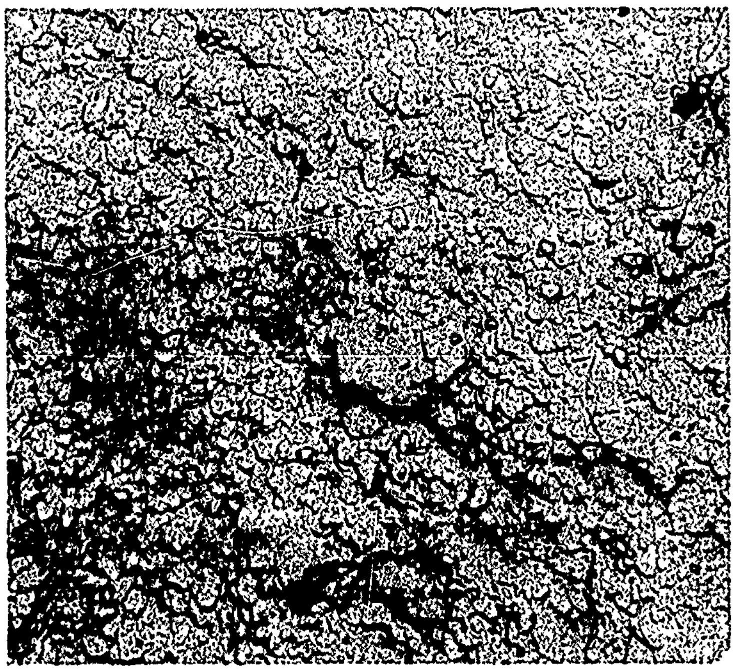

Figure 34. Appearance of the Fast Fracture Zone on Ti-Cad Specimen No. 1.
Transmission Electron Micrograph

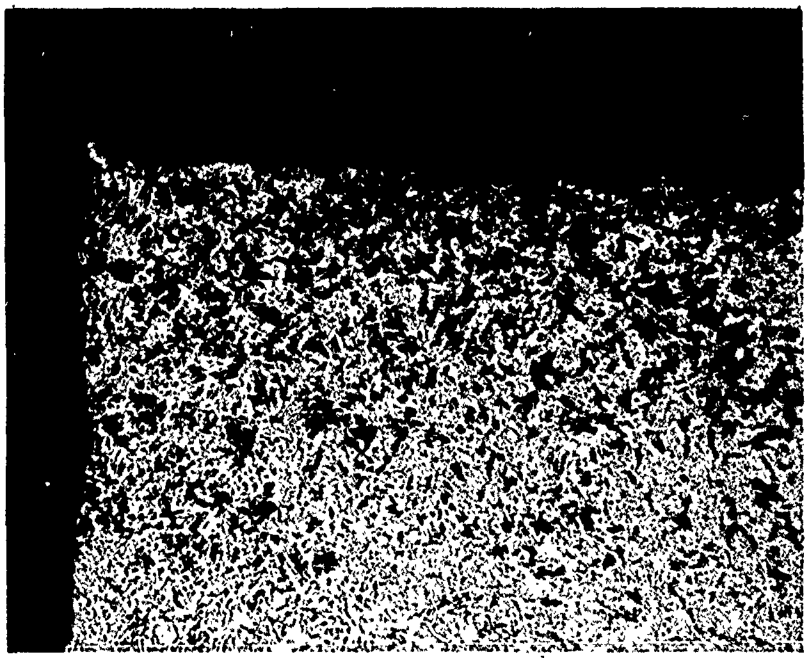

Figure 35. Photomicrograph of Cross-section Through Failure Origin of Shaft from A-7B-137. Tapered Hole at Left and Origin. Top Left a Small Shear Lip Can Be Seen at the Origin. Nital Etch

Figure 36. Cross-section Through Failure Origin of Shaft from A-7B-181. Perpendicular Crack Occured Inboard from Tapered Hole in the Transition Area from Intergranular to (Dimple) Rapid Fracture.

Figure 37. Cross Section of Failure Origin of Shaft From A-7D-8. There Appeared to Be Small Shear Lip at Extreme Edge of Origin Top-Right. Nital Etch

Figure 38. Cross-section of Failure Origin of Shaft from A-7B-121. Some Small Intergranular Cracking Can Be Seen Associated with Fracture. This Origin (Top Right) Had Been Damaged During Failure. Nital Etch

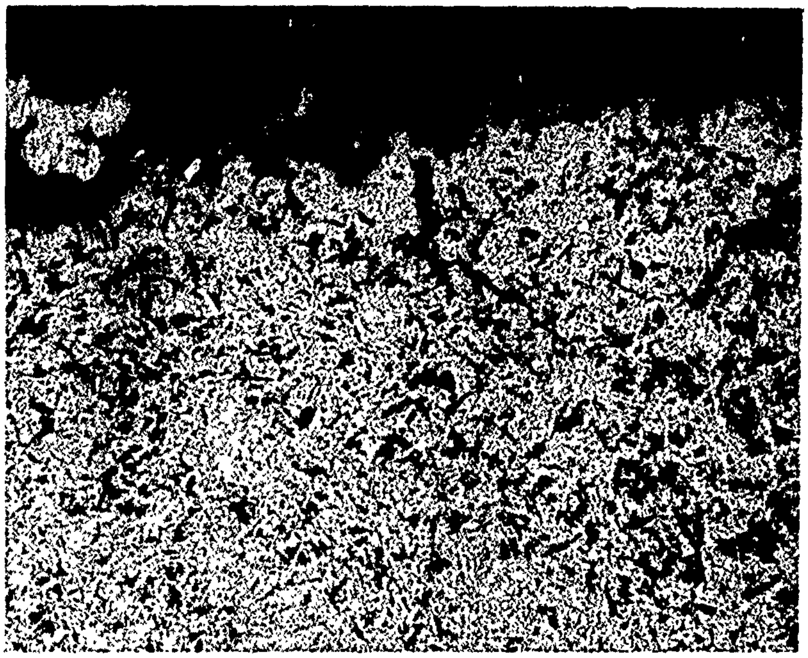

Figure 39. Cross-section of Failure Origin of Shaft from A-7B-107. Intergranular Cracks Were Associated with TE Fracture Surface in the Intergranular. Nucleus Area. Nital Etch

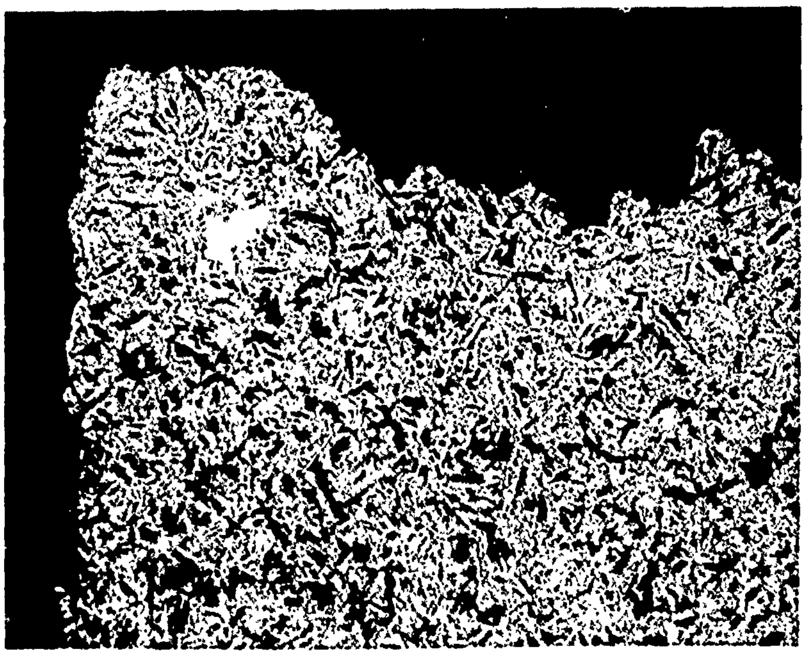

Figure 40. Cross-section of Failure Origin of Shaft from A-7B-183. No Evidence of Secondary Cracking Propagating from the Tapered Hole (Left) Was Observed on Any of the Surface Failures. Nital Etch

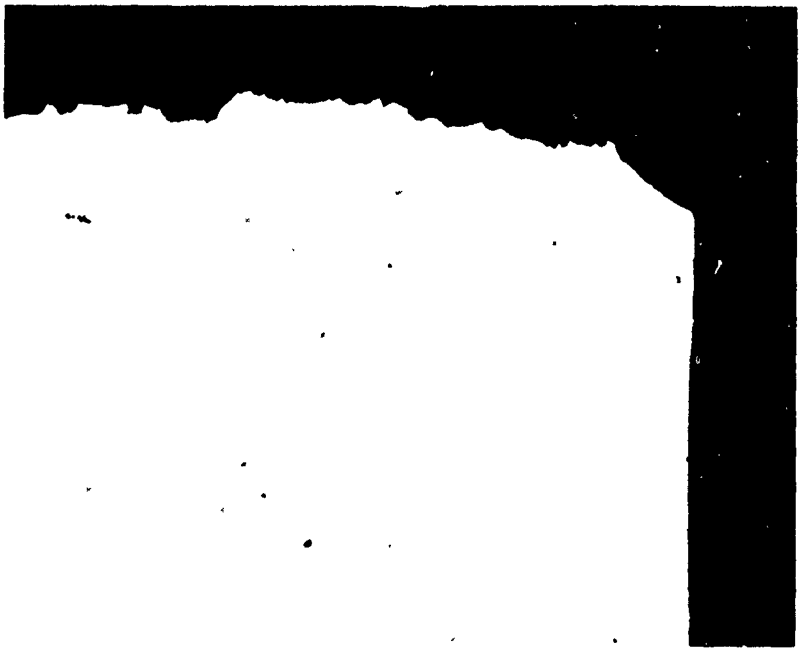

Figure 41. Cross-section of Failure Origin of Horn from A-7B-183.
A Shear Lip Can Be Seen at the Origin (Top Right).
Small Minute Cracks Are Present in the Intergranular Nucleus Area.
Unetched

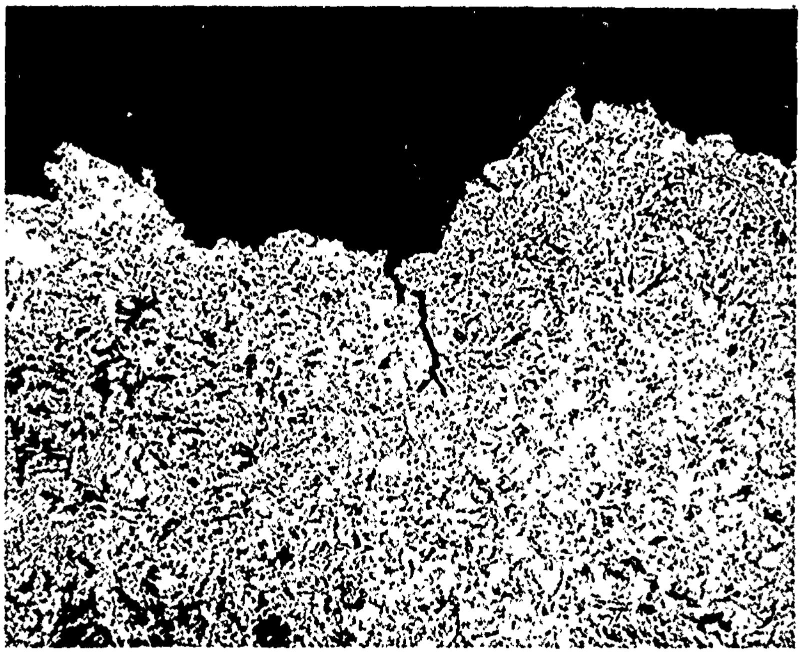

Figure 42. Enlargement of Inboard Intergranular Crack in Figure 41 Above.
Nital Etch

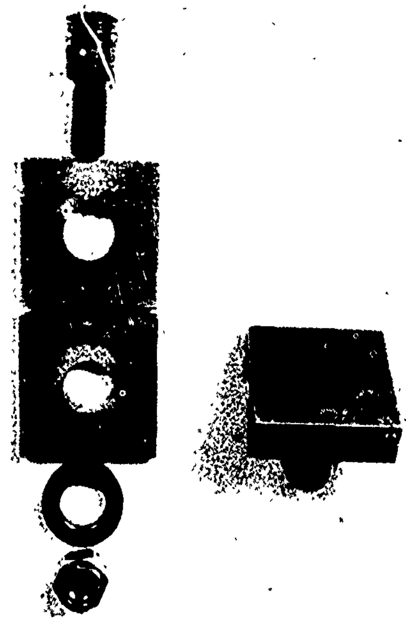

Figure 43. Photograph of Simulated UHT Horn and Shaft Test Fixtures.

Figure 44. Photomacrograph of The Fracture Surface of The Simulated Shaft After Induced Failure. The Fracture Depicts Only Tension and Shear Modes. No Evidence of Cadmium Cracking Was Observed.

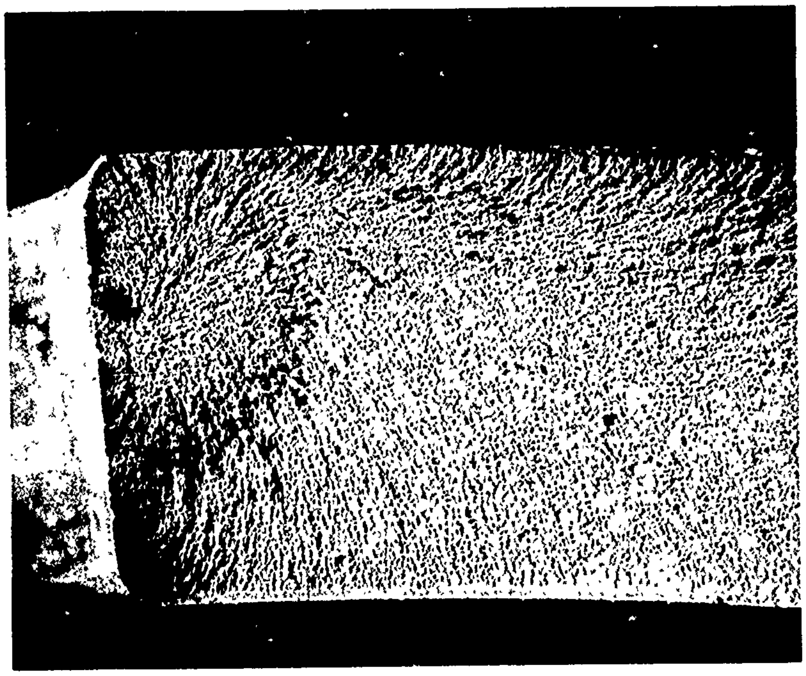

Figure 45. Fracture Origin from a UHT. Shaft Removed from A-7B-137

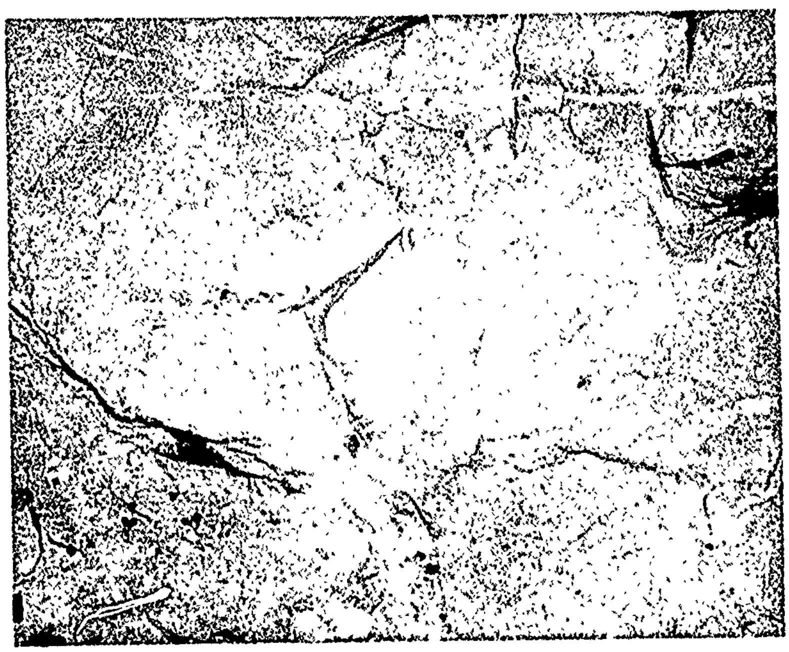

Figure 46. Fracture Appearance Near Mid-origin on Fracture from A-7B-137. Transmission Electron Micrograph

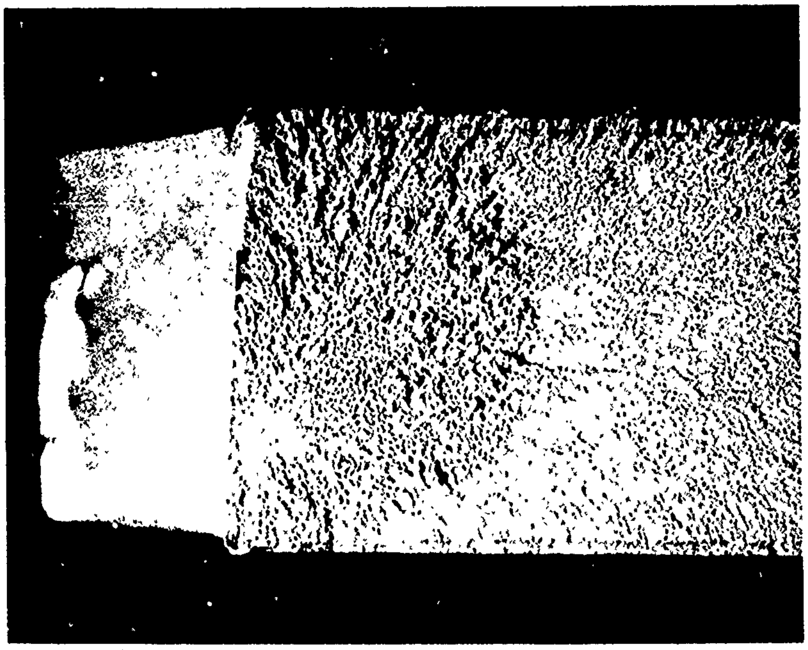

Figure 47. Fracture Origin on UHT Shaft from A-7B-107

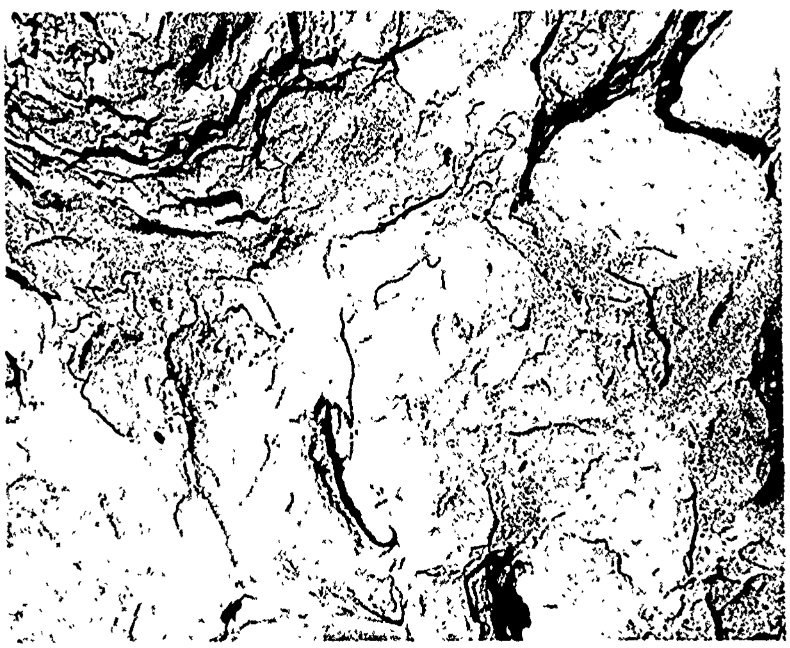

Figure 48. Fracture Appearance Near Mid-Origin on Fracture from A-7B-107. Transmission Electron Micrograph

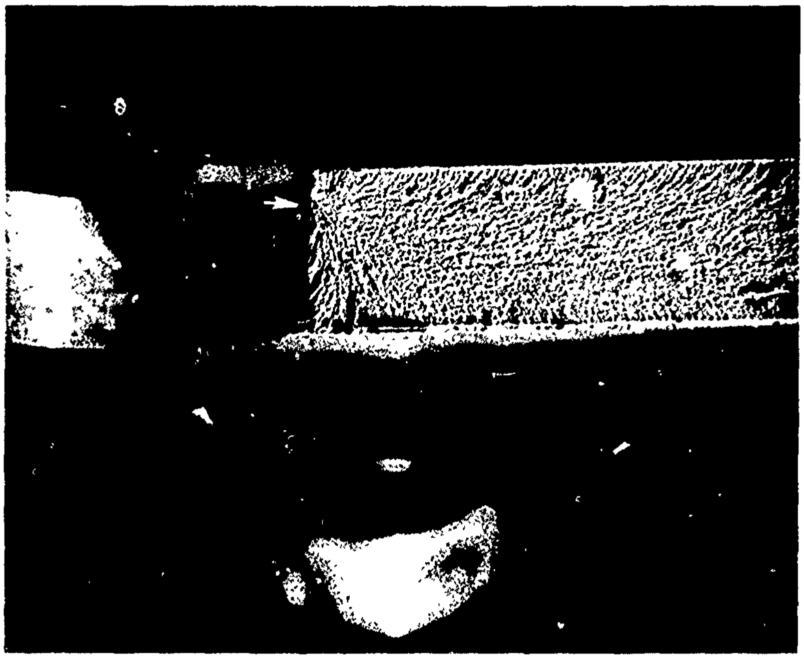

Figure 49. Fracture Origin on UHT Shaft from A-7B-121

Figure 50. Fracture Appearance Near Mid-origin on Fracture from A-7B-121. Transmission Electron Micrograph

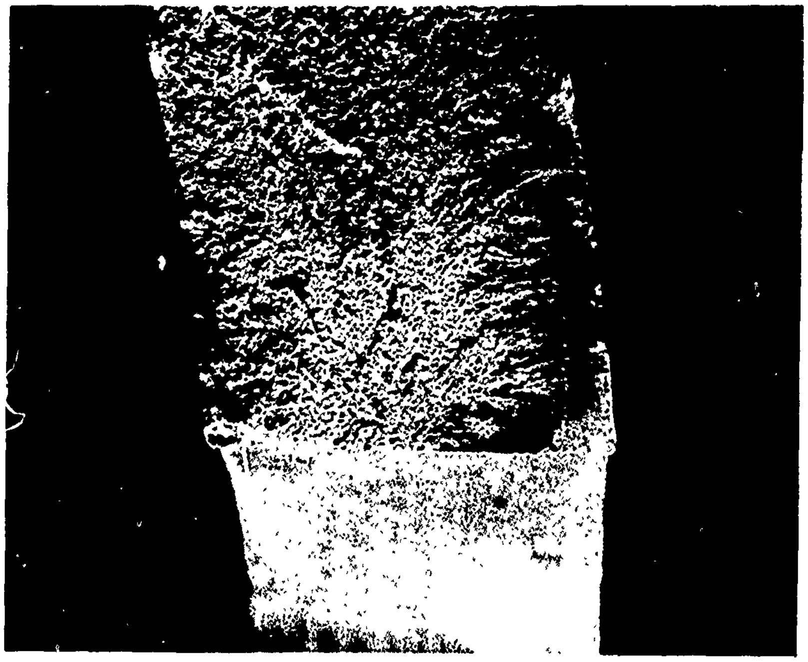

Figure 51. Fracture Origin on a UHT Horn from A-7B-183.

Figure 52. Fracture Appearance Near Mid-origin of Fracture from Horn from A-7B-183. Transmission Electron Micrograph

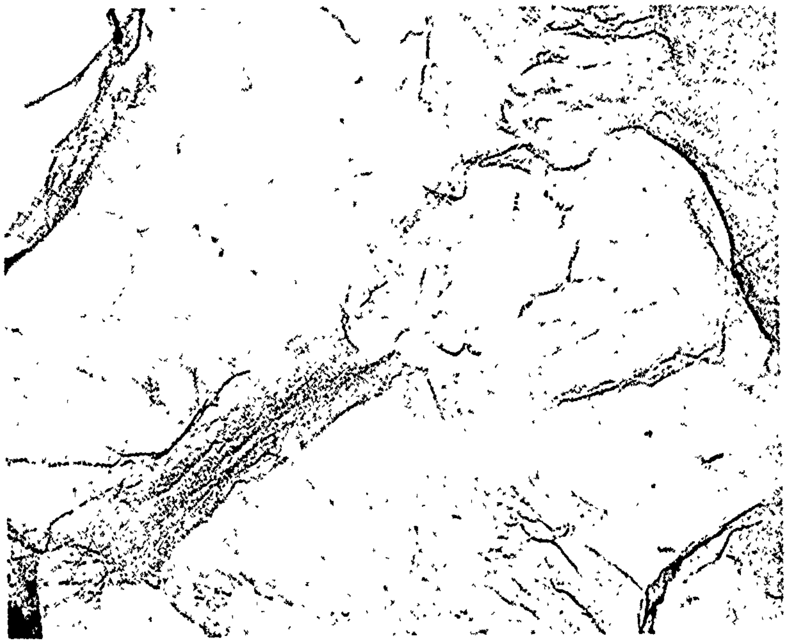

Figure 53. Fracture Origin on UHT Shaft from A-7D-8

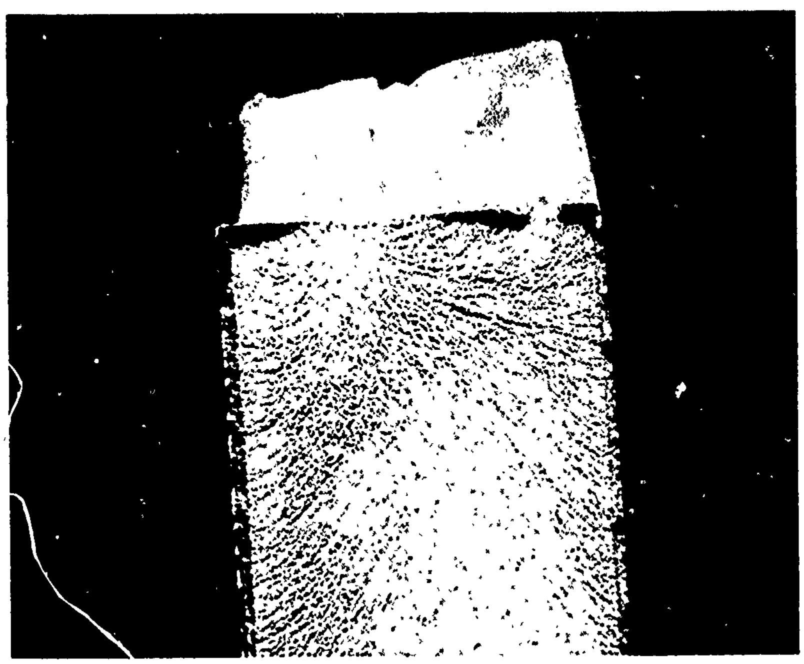

Figure 54. Fracture Appearance Near Mid-origin on Fracture from A-7D-8. Transmission Electron Micrograph

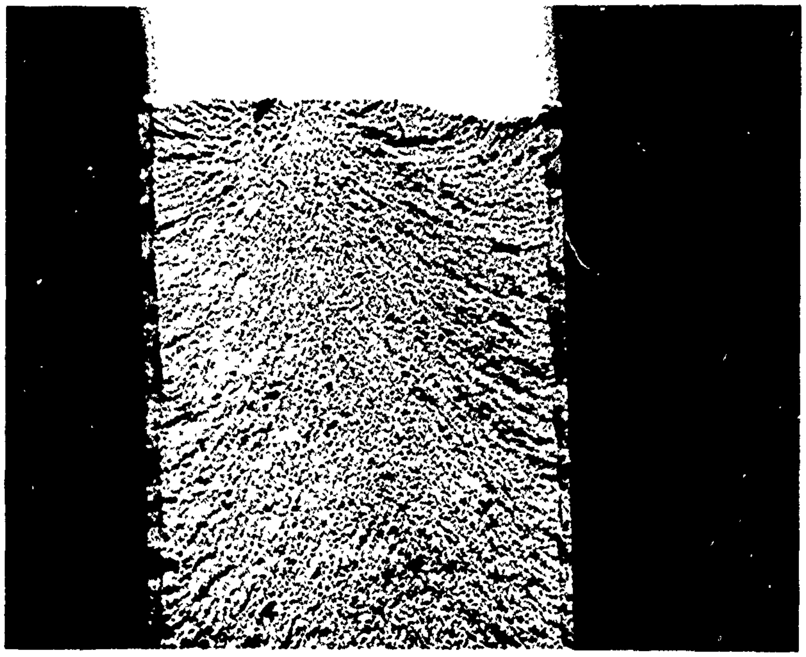

Figure 55. Fracture Origin on UHT Shaft from A-7B-181.

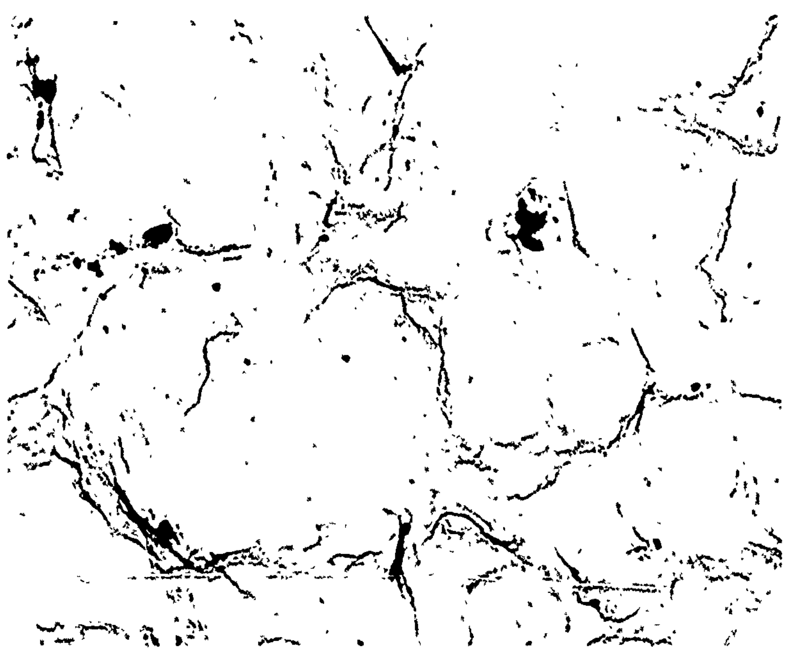

Figure 56. Fracture Appearance Near Mid-origin of Fracture from A-7B-181. Transmission Electron Micrograph

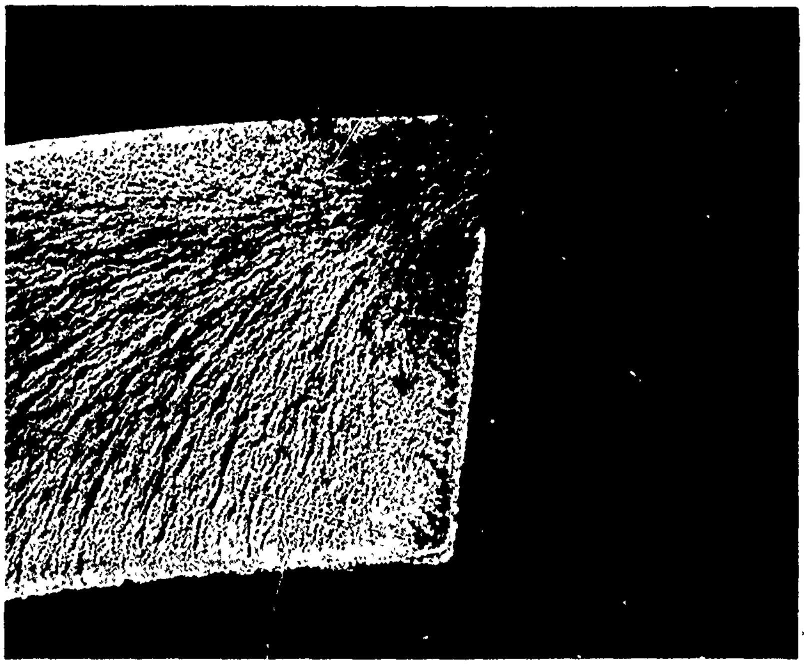

Figure 57. Fracture Origin on UHT Shaft from A-7B-183.

Figure 58. Fracture Appearance Near Mid-orgin of the Shaft Fracture from A-7B-183. Transmission Electron Micrograph

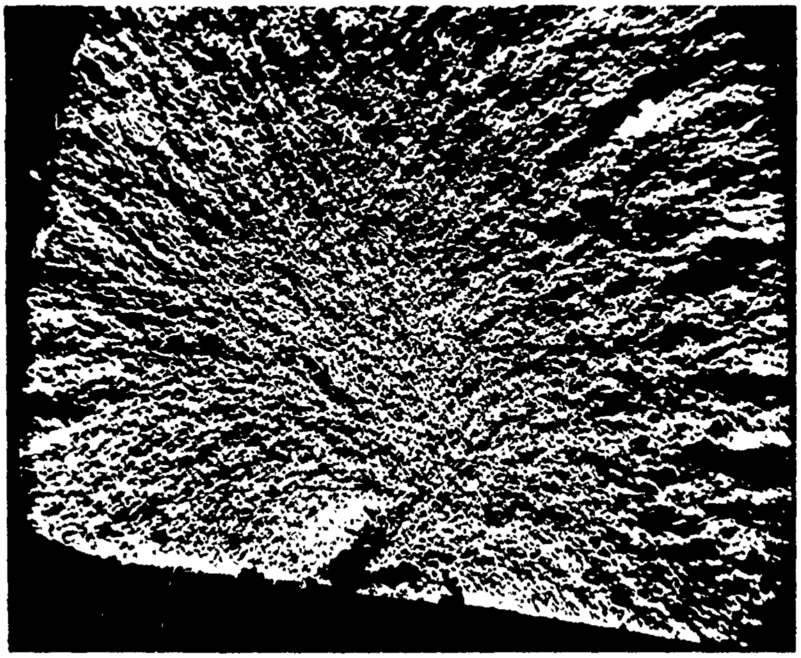

Figure 59. Fracture Origin on UHT Shaft from A-7B-137. Note the Shear Lip Along the Edge at the Hole, Lowermost. Backscatter Electron Image

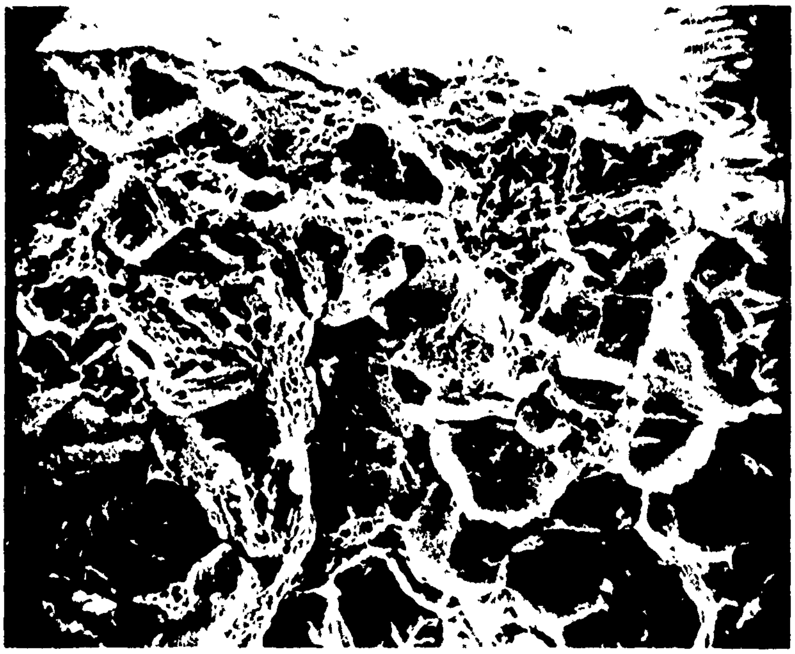

Figure 60. Fracture Appearance Adjacent to the Hole on UHT Shaft Fracture from A-7B-137. Note Shear Lip at Surface, Uppermost. Scanning Electron Micrograph

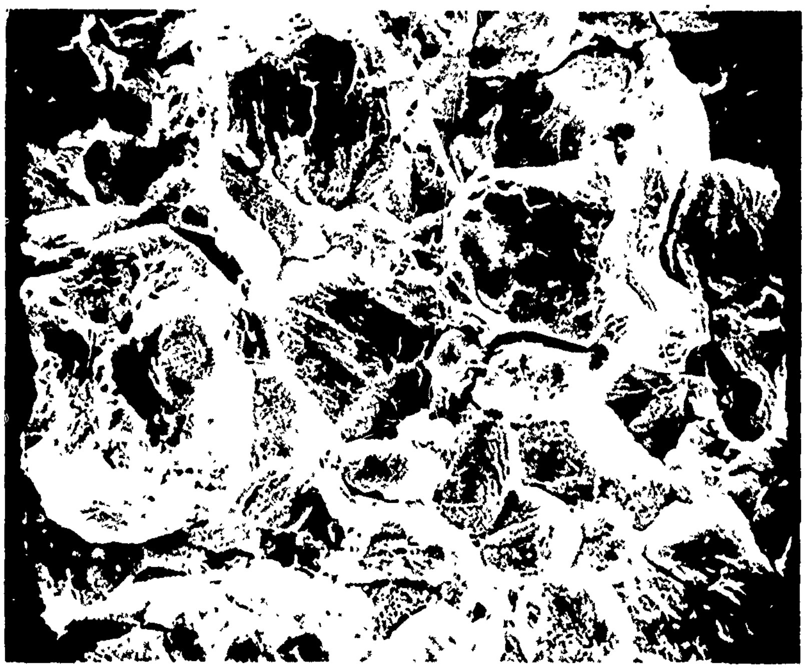

Figure 61. Fracture Appearance Near Mid-origin on Fracture from A-7B-137. Note Hairline Crack Indications on Grain Facets. Scanning Electron Micrograph

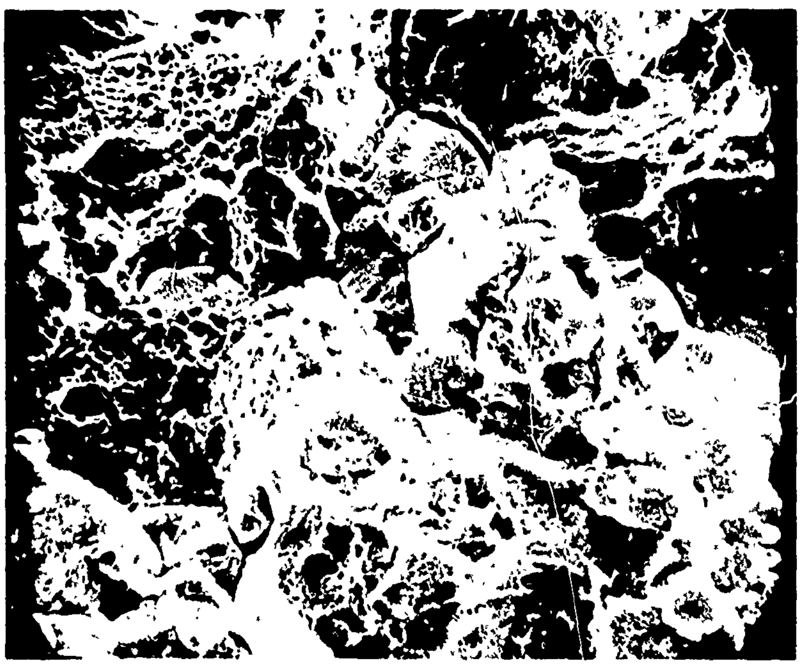

Figure 62. Fracture Appearance in the Transition to Rapid Fracture Zone on the Fracture from A-7B-137. Scanning Electron Micrograph

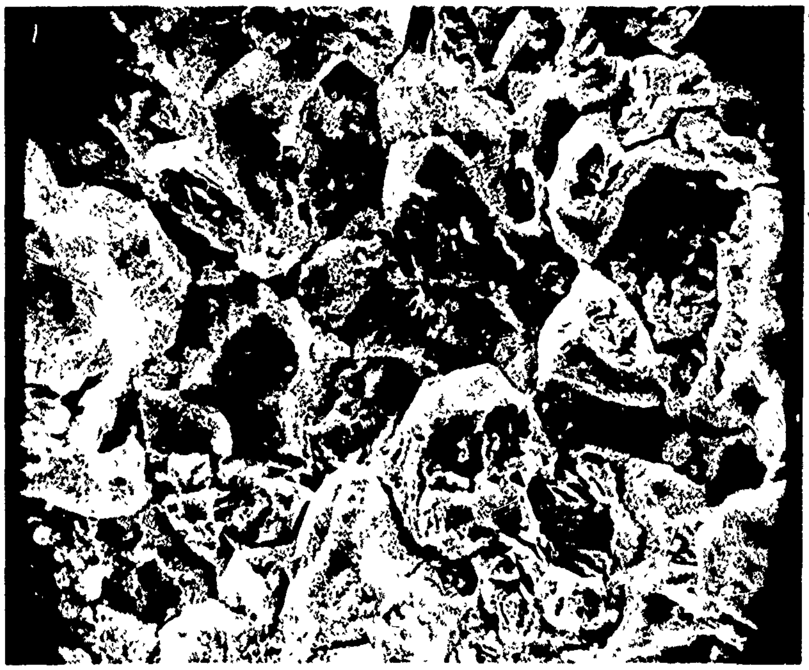

Figure 63. Fracture Appearance Adjacent to the Pinhole on the Fracture from A-7D-8. Scanning Electron Micrograph

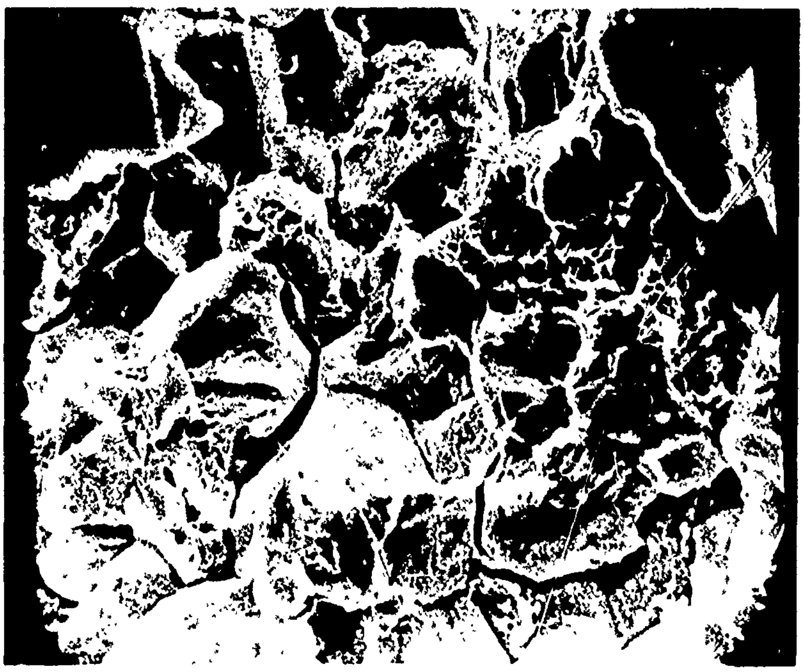

Figure 64. Fracture Appearance Near Mid-origin on Fracture from A-7D-8. Scanning Electron Micrograph

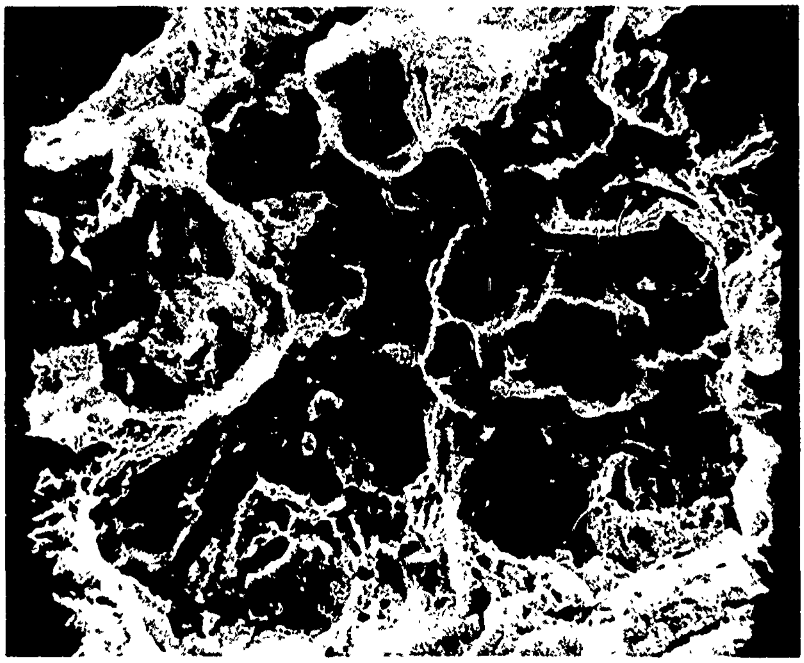

Figure 65. Fracture Appearance Near the Onset of Rapid Fracture on the Fracture from A-7D-8. Scanning Electron Micrograph

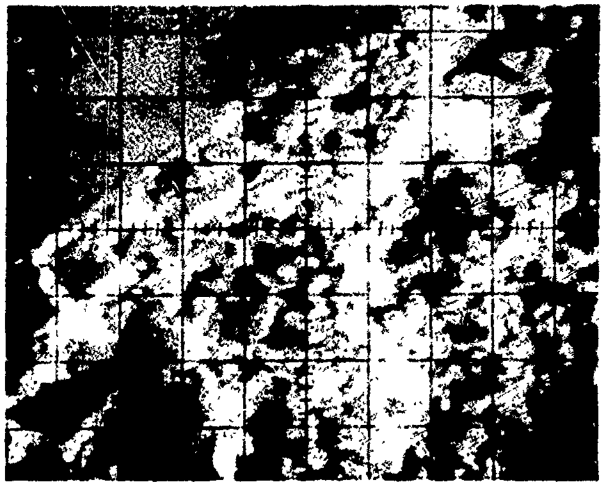

Figure 66. Backscattered Electron Image of Origin, Induced Cadmium-embrittled Fracture. ARL Probe.

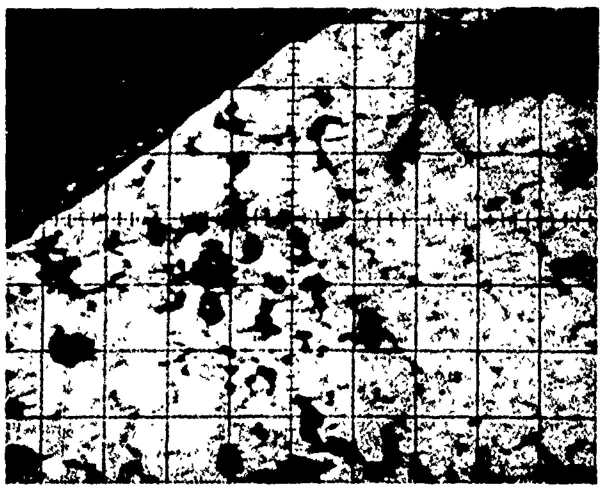

Figure 67. Secondary Electron Image of Origin, Induced Cadmium-embrittled Fracture. ARL Probe

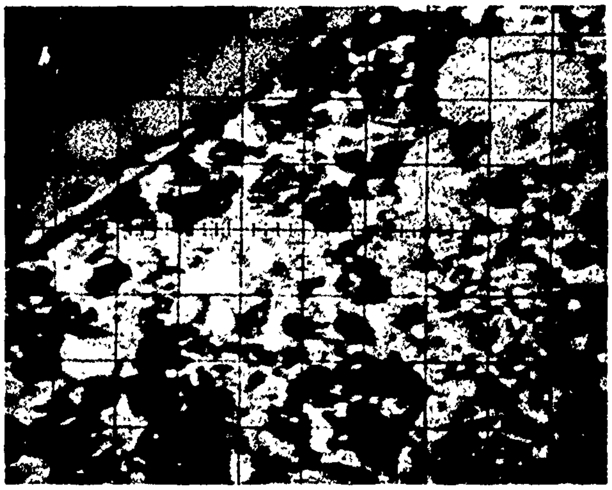

Figure 68. Specimen Current Image of Origin, Induced Cadmium-embrittled Fracture. ARL Probe

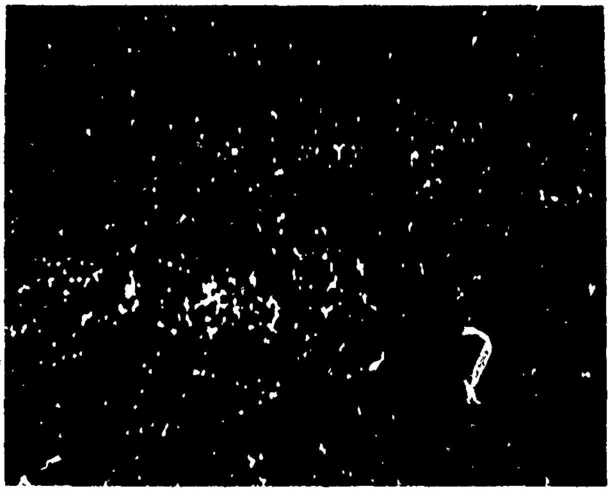

Figure 69. Cadmium X-ray Distribution Map of Origin, Induced Cadmium-embrittled Fracture. ARL Probe

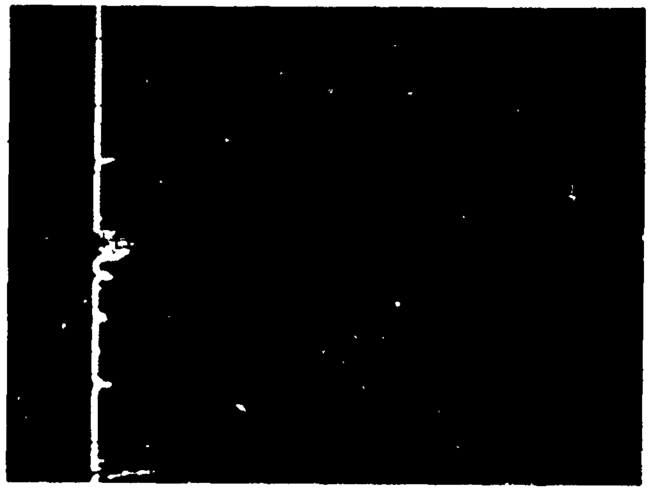

Figure 70. Cadmium Concentration Profile Measured Down the Vertical Hatched Center Line Shown in Figure 66.

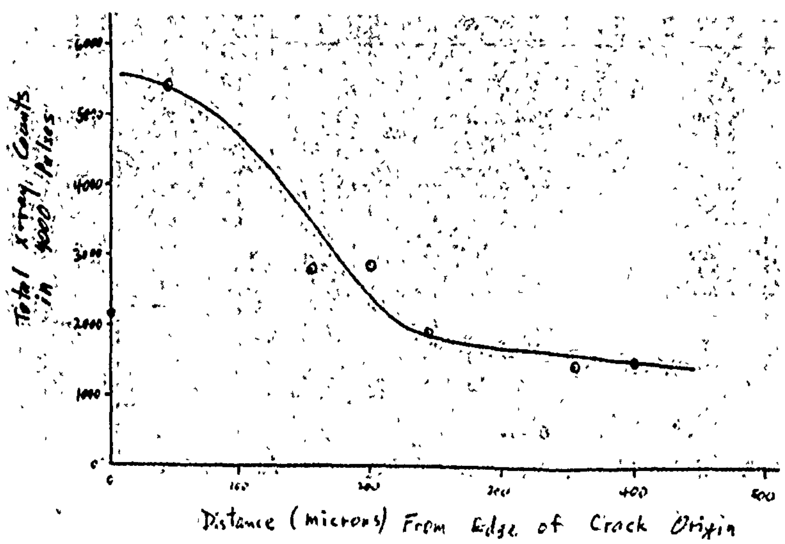

Figure 71. Cadmium Concentration Gradient as Revealed by Point Counts Along Fracture Surface Showing in from Cadmium-plated Edge.

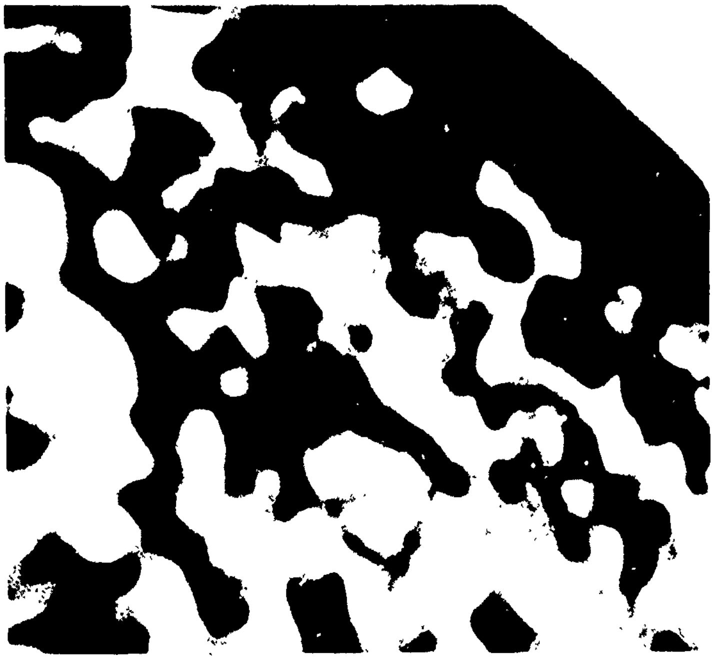

Figure 72. Backscattered and Secondary Electron Scan of Origin, Induced Cadmium-embrittled Fracture. CAMECA Probe

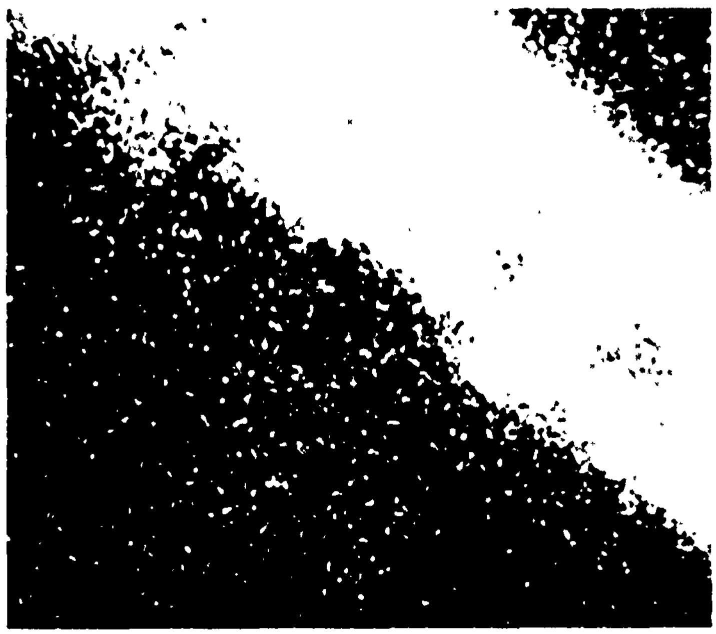

Figure 73. Cadmium X-ray Distribution Map of Origin, Induced Cadmium-embrittled Fracture. CAMECA Probe

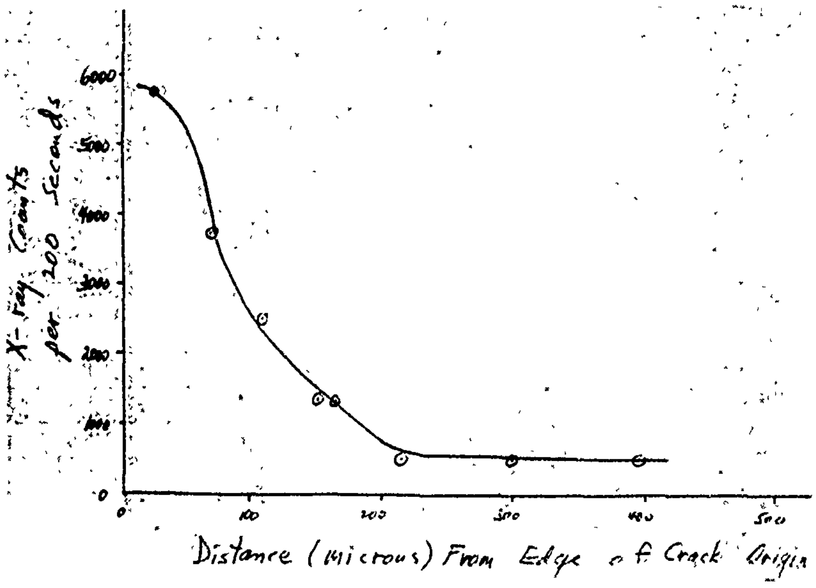

Figure 74. Cadmium Concentration Gradient as Revealed by Point Counts Along Fracture Surface Moving in from Cadmium-plated Edge.

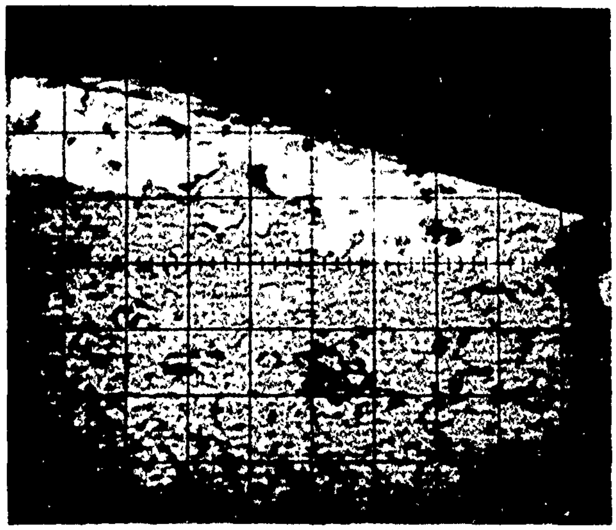

Figure 75. Backscattered Electron Image of Origin, UHT Shaft from A-7B-121. ARL Probe

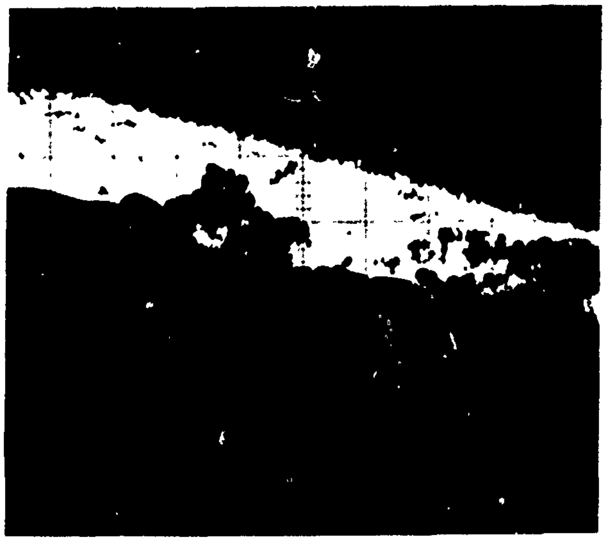

Figure 76. Cadmium X-ray Distribution Map of Origin, UHT Shaft from A-7B-121. ARL Probe

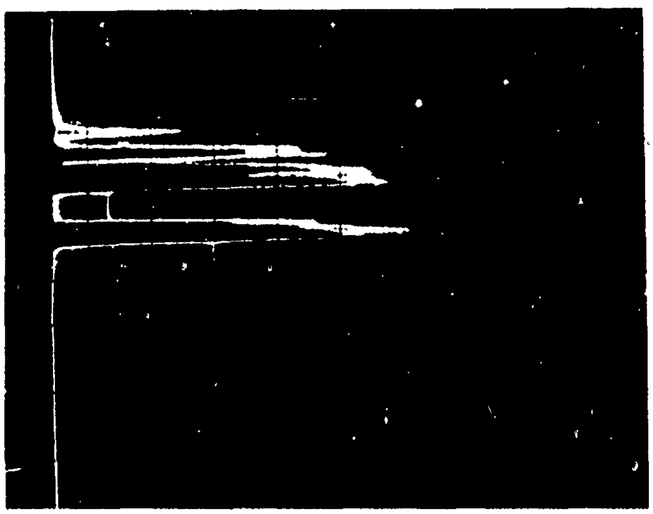

Figure 77. Cadmium Concentration Profile Measured Down the Vertical Batched Centerline Shown in Figure 75.

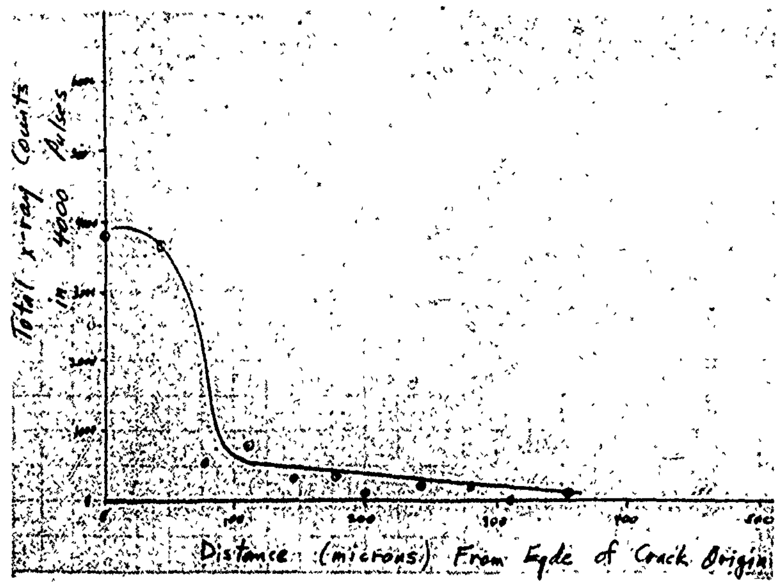

Figure 78. Cadmium Concentration Gradient as Revealed by Point Counts Along Fracture Surface Moving in from the Cadmium-plated Edge, A-7B-121.

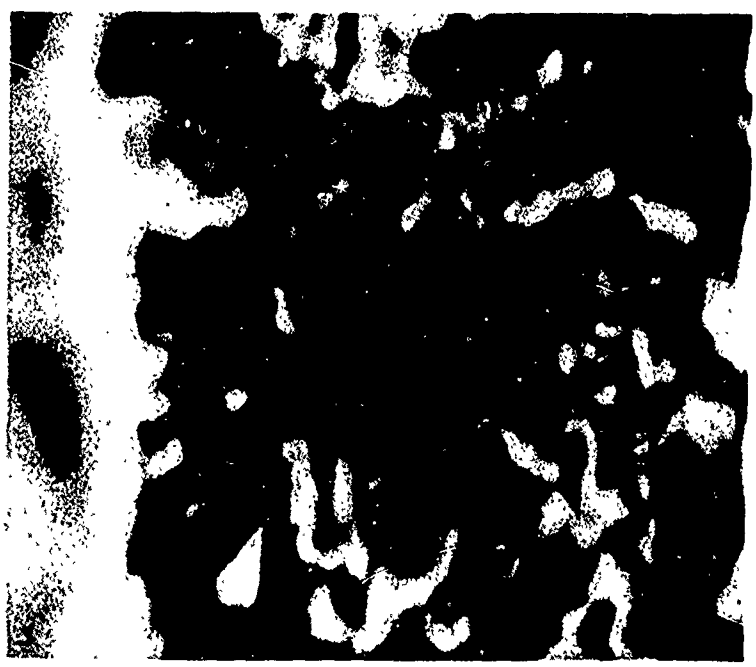

Figure 79. Backscattered and Secondary Electron Scan of Origin, Shaft from A-7B-121. CAMECA Probe.

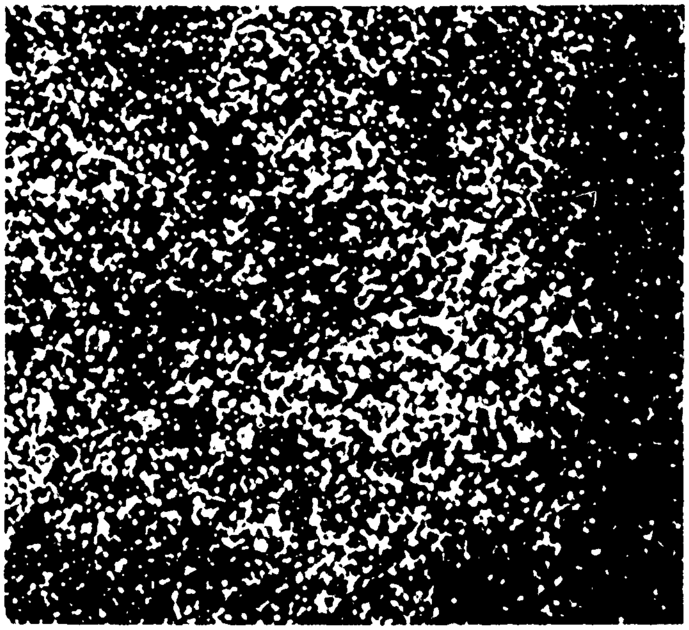

Figure 80. Cadmium X-ray Distribution Map of Origin, Shaft from A-7B-121. CAMECA Probe.

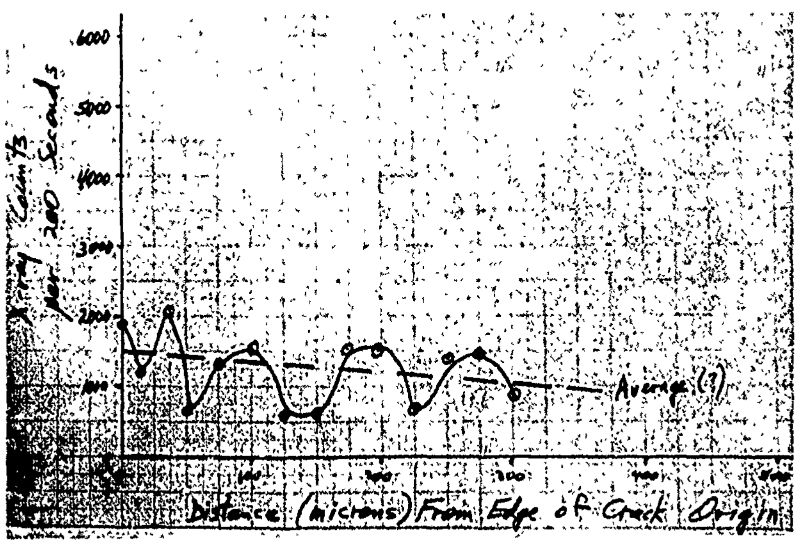

Figure 81. Cadmium Concentration Gradient as revealed by Point Counts Along Fracture Surface Moving in from Cadmium-plated Edge at Right.

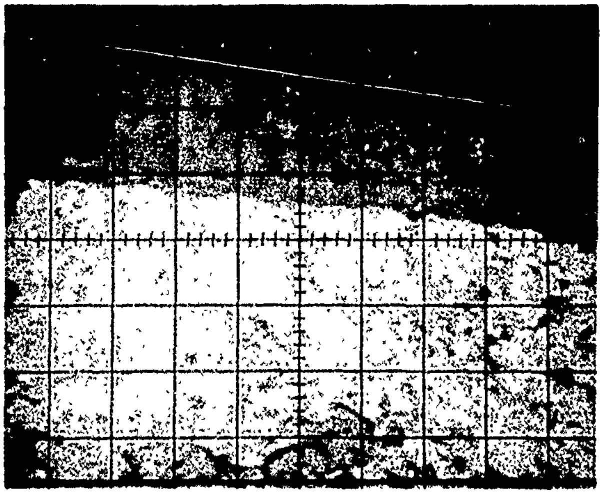

Figure 82. Backscattered Electron Image of Origin, Shaft from A-7B-107. ARL Probe

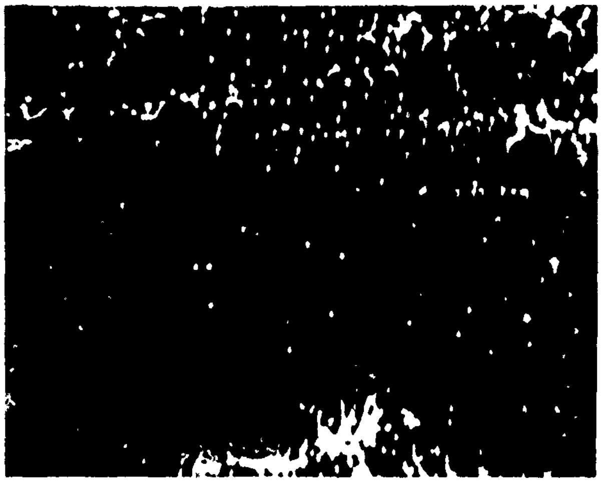

Figure 83. Cadmium X-ray Distribution Map of Origin, Shaft from A-7B-107. ARL Probe

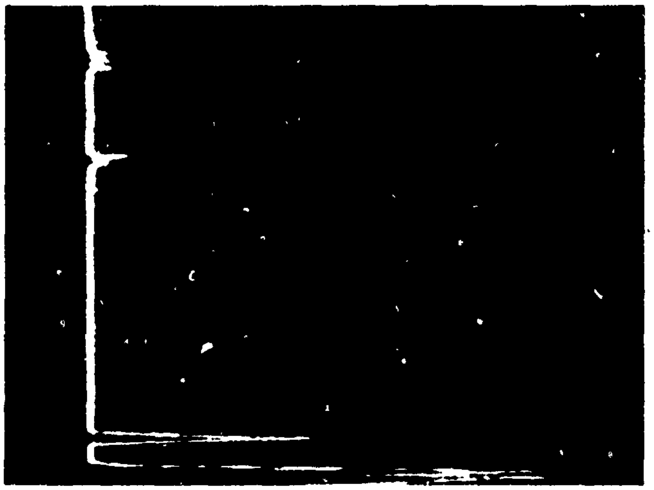

Figure 84. Cadmium Concentration Profile Measured Down the Vertical Batched Center Line Shown in Figure 82. ARL Probe

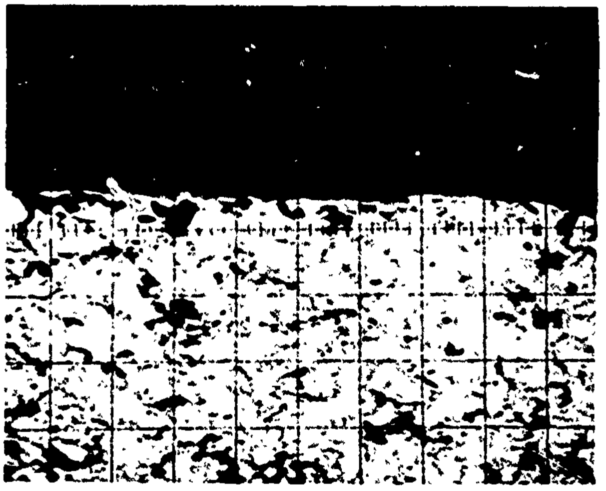

Figure 85. Backscattered Electron Image of Origin, Shaft from A-7B-137. ARL Probe

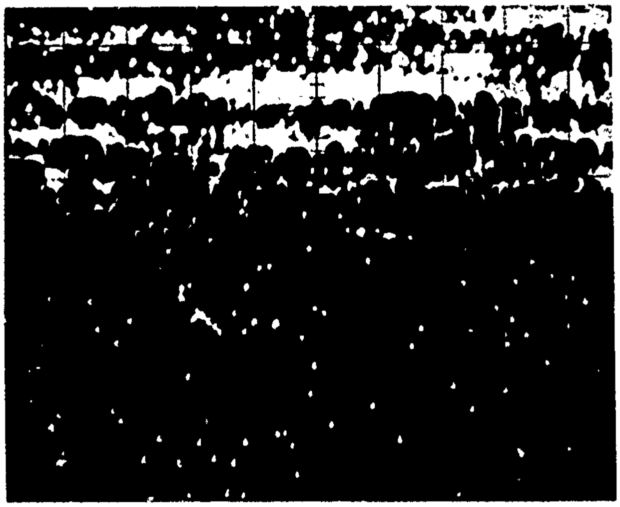

Figure 86. Cadmium X-ray Distribution Map of Origin, Shaft from A-7B-137. ARL Probe

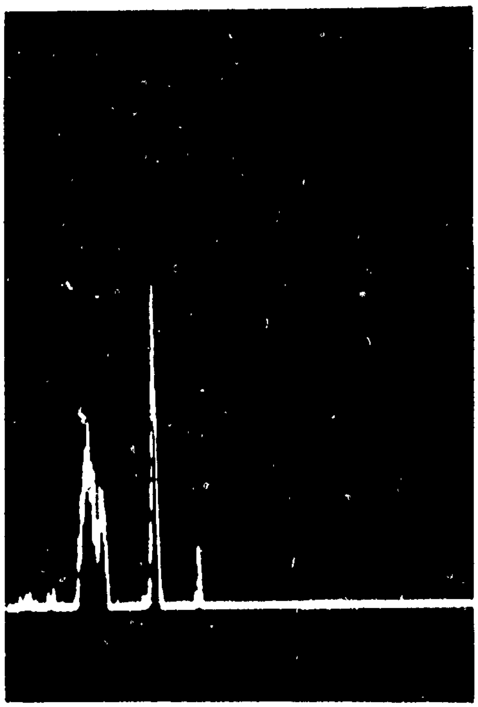

Figure 87. Cadmium Concentration Profile Measured Down the Vertical Batched Center Line Shown in Figure 85. ARL Probe

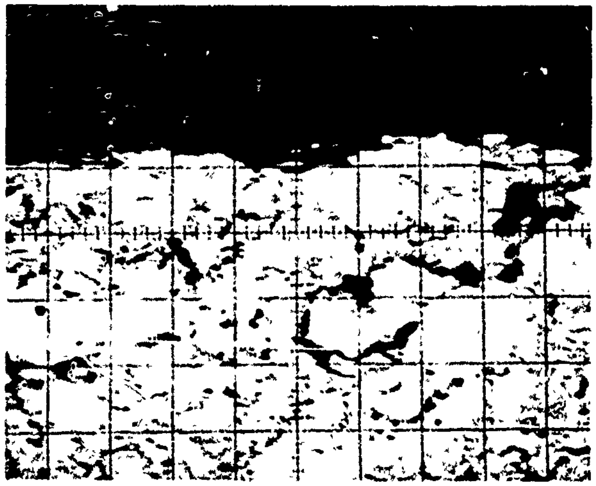

Figure 88. Backscattered Electron Image of Origin, Shaft from A-7B-183. ARL Probe.

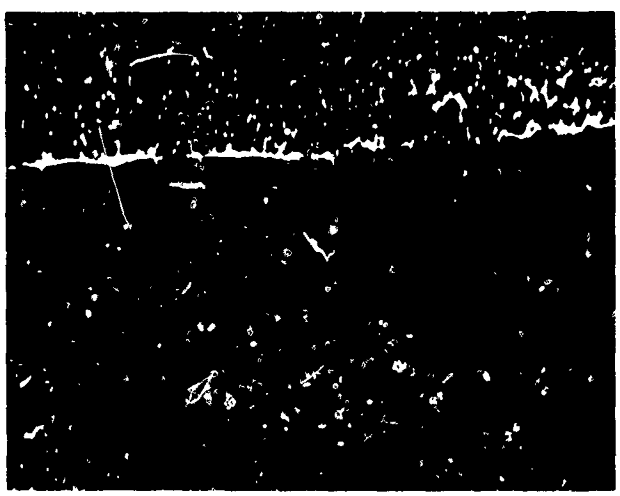

Figure 89. Cadmium X-ray Distribution Map of Same Area Shown in Figure 88. ARL Probe

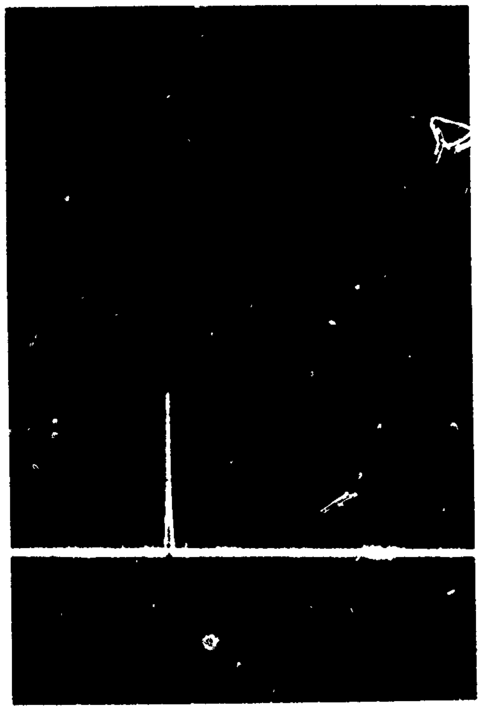

Figure 90. Cadmium Concentration Profile Measured Along Vertical Centerline Shown in Figure 88.

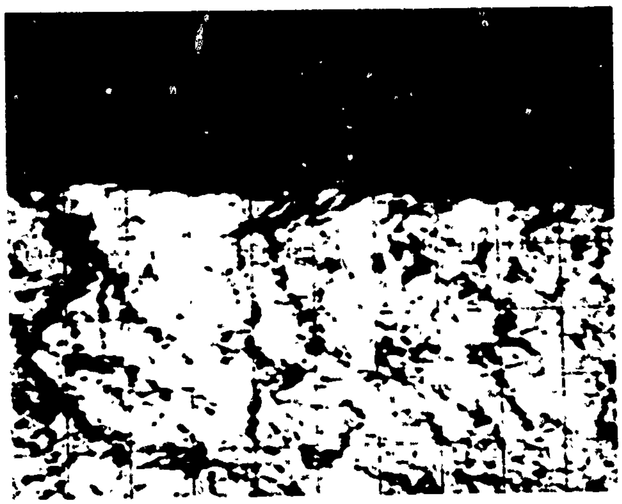

Figure 91. Backscattered Electron Image of Origin, Shaft from A-7D-8. ARL Probe.

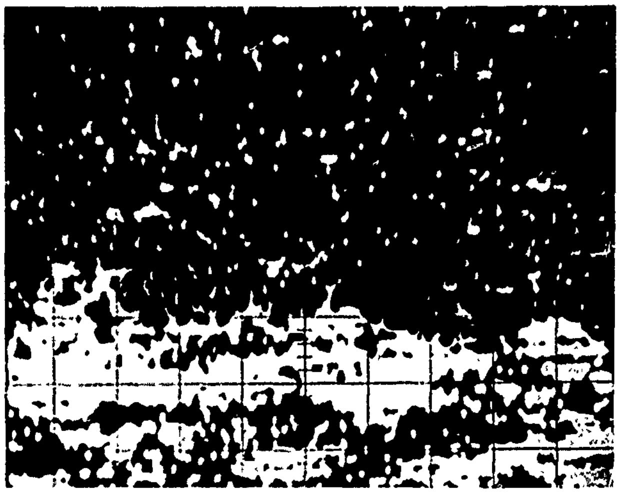

Figure 92. Cadmium X-ray Distribution Map of Same Area Shown in Figure 91. ARL Probe.

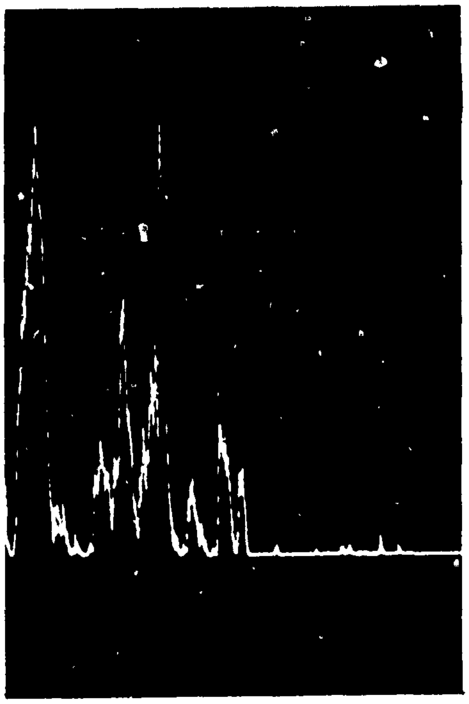

Figure 93. Cadmium Concentration Profile Measured Along the Vertical Centerline Shown in Figure 91. ARL Probe

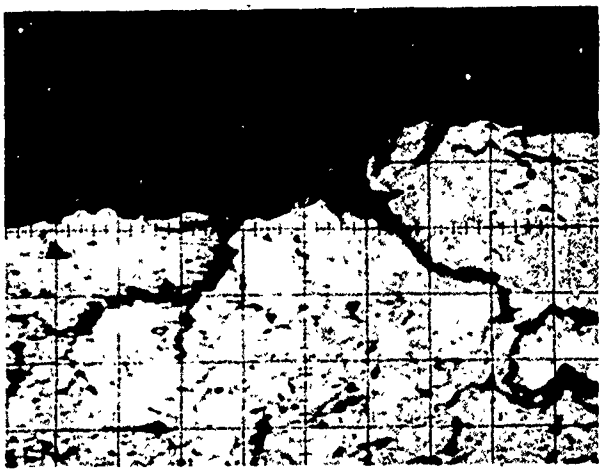

Figure 94. Backscattered Electron Image of Origin, Shaft from A-7B-181. ARL Probe.

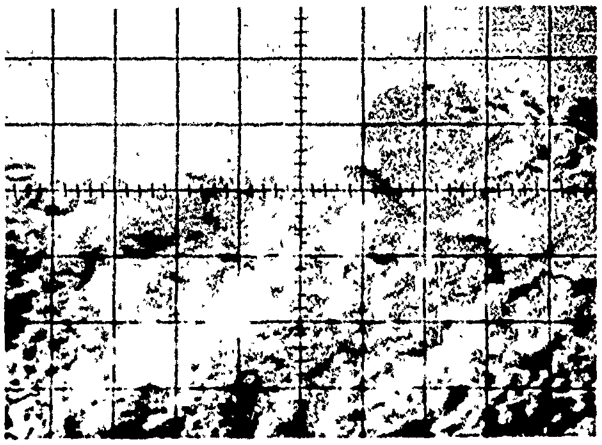

Figure 95. Secondary Electron Image of Origin, Shaft from A-7B-181. ARL Probe.

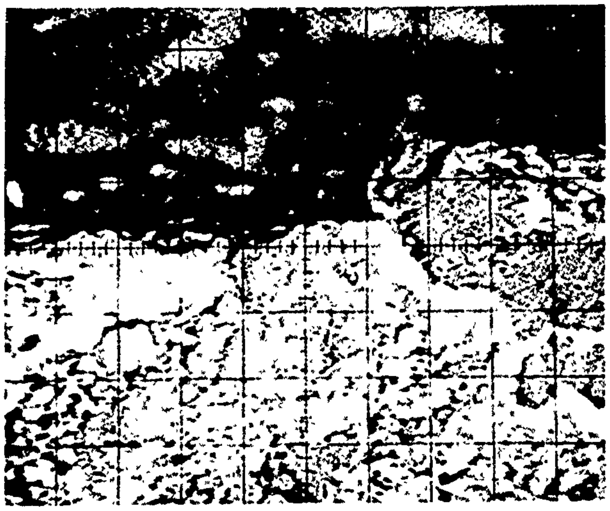

Figure 96. Specimen Current Image of Origin, Shaft from A-7B-181. ARL Probe.

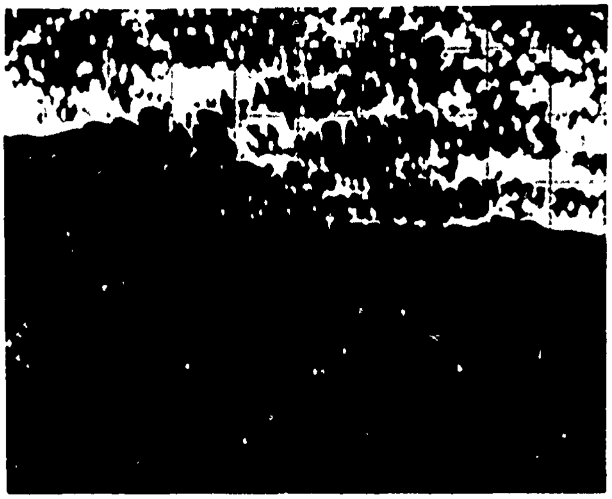

Figure 97. Cadmium X-rav Distribution Map of Origin, Shaft from A-7B-181. /RL Probe

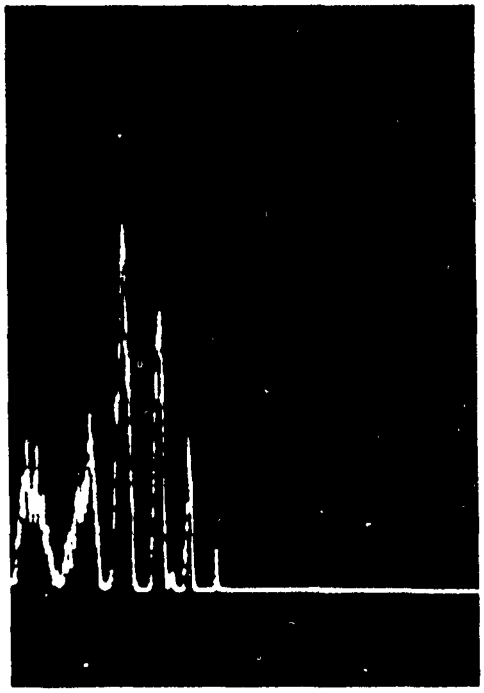

Figure 98. Cadmium Concentration Profile Measured Down the Vertical Centerline in Figure 95.

Figure 99. Backscattered Electron Image of Origin, UHT Horn from A-7B-183. ARL Probe.

Figure 100. Cadmium X-ray Distribution Map of Origin, UHT Horn from A-7B-183. ARL Probe

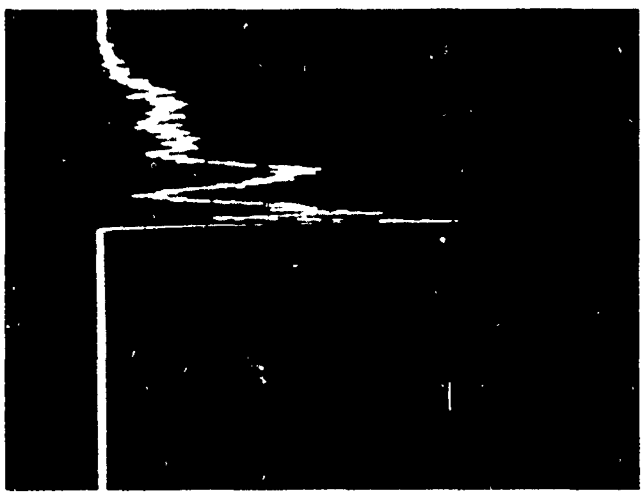

Figure 101. Cadmium Concentration Profile Measured Down the Vertical Hatched Line in Figure 99.

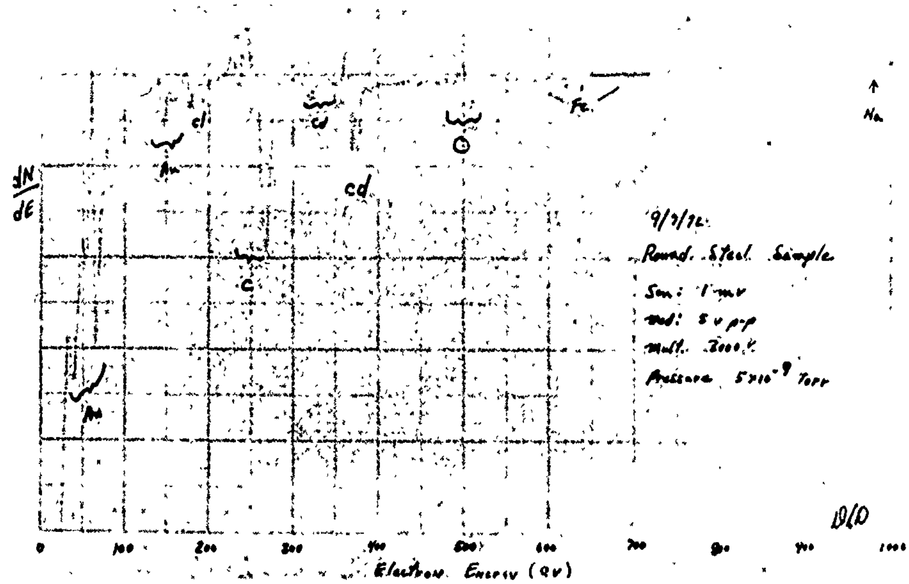

Figure 102. Auger Spectrum of Induced Cadmium-embrittled Fracture.

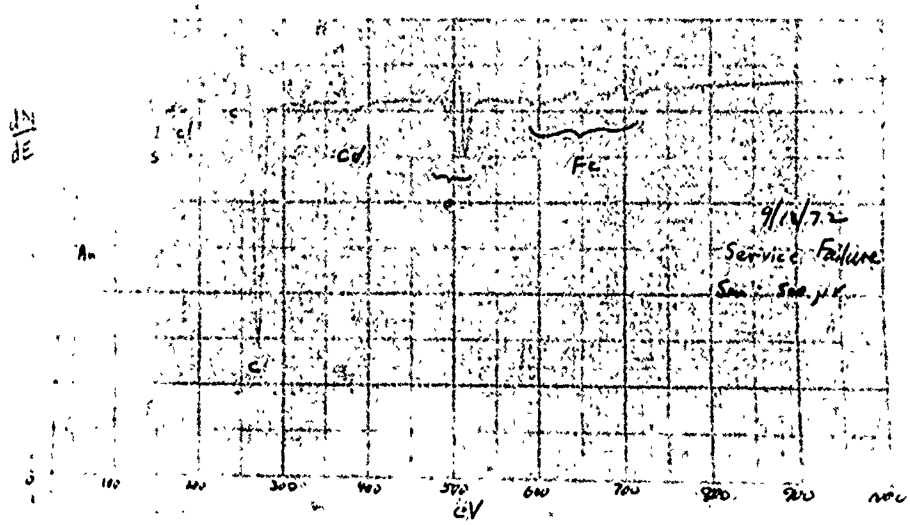

Figure 103. Auger Spectrum of In-service Fracture.